Satellite observations of atmospheric methane and their value for quantifying methane emissions

Daniel J. Jacob (djacob@fas.harvard.edu)[1], Alexander J. Turner[1], Joannes D. Maasakkers[1], Jianxiong Sheng[1], Kang Sun[2], Xiong Liu[2], Kelly Chance[2], Ilse Aben[3], Jason McKeever[4], Christian Frankenberg[5]

[1]School of Engineering and Applied Sciences, Harvard University, Cambridge, Massachusetts USA
[2] Smithsonian Astrophysical Observatory, Cambridge, Massachusetts USA
[3] SRON Netherlands Institute for Space Research, Utrecht, Netherlands
[4] GHGSat, Inc., Montreal, Canada
[5] California Institute of Technology, Pasadena, California USA

submitted to *Atmospheric Chemistry and Physics,* June 24, 2016
revised, October 31, 2016

Abstract

Methane is a greenhouse gas emitted by a range of natural and anthropogenic sources. Atmospheric methane has been measured continuously from space since 2003, and new instruments are planned for launch in the near future that will greatly expand the capabilities of space-based observations. We review the value of current, future, and proposed satellite observations to better quantify and understand methane emissions through inverse analyses, from the global scale down to the scale of point sources and in combination with suborbital (surface and aircraft) data. Current global observations from GOSAT are of high quality but have sparse spatial coverage. They can quantify methane emissions on a regional scale (100-1000 km) through multi-year averaging. TROPOMI to be launched in 2017 is expected to quantify daily emissions on the regional scale and will also effectively detect large point sources. A different observing strategy attempted by GHGSat (launched in June 2016) is to target limited viewing domains with very fine pixel resolution in order to detect a wide range of methane point sources. Geostationary observation of methane, still in the proposal stage, will have unique capability for mapping source regions with high resolution, detecting transient "super-emitter" point sources, and resolving diurnal variation of emissions from sources such as wetlands and manure. Exploiting these rapidly expanding satellite measurement capabilities to quantify methane emissions requires a parallel effort to construct high-quality spatially and sectorally resolved emission inventories. Partnership between top-down inverse analyses of atmospheric data and bottom-up construction of emission inventories is crucial to better understand methane emission processes and from there to inform climate policy.

1. Introduction

Methane is a greenhouse gas emitted by anthropogenic sources including livestock, oil/gas systems, landfills, coal mines, wastewater management, and rice cultivation. Wetlands are the dominant natural source. The atmospheric concentration of methane has risen from 720 to 1800 ppb since pre-industrial times (Hartmann et al., 2013). The resulting radiative forcing on an emission basis is 0.97 W m^{-2}, compared to 1.68 W m^{-2} for CO_2 (Myhre et al., 2013). The present-day global emission of methane is well-known to be 550 ± 60 Tg a^{-1}, as inferred from mass balance with the global methane sink from oxidation by OH radicals (Prather et al., 2012). However, the contributions from different source sectors and source regions are highly uncertain (Dlugokencky et al., 2011; Kirschke et al., 2013). Emission inventories used for climate policy rely on "bottom-up" estimates of activity rates and emission factors for individual source processes. "Top-down" information from observations of atmospheric methane is often at odds with these estimates and differences need to be reconciled (Brandt et al., 2014). Satellite observations of atmospheric composition have emerged over the past decade as a promising resource to infer emissions of various gases (Streets et al., 2013). Here we review present, near-future, and proposed satellite observations of atmospheric methane and assess their value for quantifying emissions, from regional scales down to the scale of individual point sources.

The United Nations Framework Convention on Climate Change (UNFCCC) requires individual countries to report their annual anthropogenic greenhouse gas emissions following bottom-up inventory guidelines from the International Panel on Climate Change (IPCC, 2006). As an example, Figure 1 shows the US anthropogenic methane emission inventory for 2012 compiled by the Environmental Protection Agency (EPA, 2016) and reported to the UNFCCC. The inventory uses advanced IPCC Tier 2/3 methods (IPCC, 2006) with detailed sectoral information. However, atmospheric observations from surface sites and aircraft suggest that US emissions are underestimated, and that sources from natural gas and livestock are likely responsible (Miller et al., 2013; Brandt et al., 2014). Not included in Figure 1 are wetland emissions, estimated to be 8.5 ± 5.5 Tg a^{-1} for the contiguous US (Melton et al., 2013). The global distribution of wetland emissions is extremely uncertain (Bloom et al., 2016) and quantifying these emissions through atmospheric observations is of critical importance.

Targeted atmospheric measurements of methane can quantify emissions on small scales (point source, urban area, oil/gas basin) by measuring the ratio of methane to a co-emitted species whose emission is known (Wennberg et al., 2012) or by using a simple mass balance approach (Karion et al., 2013, 2015; Peischl et al., 2013, 2016; Conley et al., 2016). Quantifying emissions on larger scales, with many contributing sources, requires a more general approach where an ensemble of atmospheric observations is fit to a 2-D field of emissions by inversion of a 3-D chemical transport model (CTM) that relates emissions to atmospheric concentrations. This inversion is usually done by Bayesian optimization accounting for errors in the CTM, in the observations, and in the prior knowledge expressed by the bottom-up inventory. We obtain from the inversion a statistically optimized emission field, and differences with the bottom-up inventory point to areas where better understanding of processes is needed. A large number of inverse studies have used surface and aircraft observations to quantify methane emissions on regional to global scales (Bergamaschi et al., 2005; Bousquet et al., 2011; Miller et al., 2013; Bruhwiler et al., 2014).

Satellites provide global and dense data that are particularly well suited for inverse analyses. Measurement of methane from space began with the IMG thermal infrared instrument in 1996-1997 (Clerbaux et al., 2003). Measurement of total methane columns by solar backscatter began with SCIAMACHY in 2003-2012 (Frankenberg et al., 2006) and continues to the present with GOSAT launched in 2009 (Kuze et al., 2016). Satellite measurements of atmospheric methane have been used to detect emission hotspots (Worden et al., 2012; Kort et al., 2014; Marais et al., 2014; Buchwitz et al., 2016) and to estimate emission trends (Schneising et al., 2014; Turner et al., 2016). They have been used in global inverse analyses to estimate emissions on regional scales (Bergamaschi et al., 2007, 2009, 2013; Monteil et al., 2013; Cressot et al., 2014; Wecht et al., 2014a; Alexe et al., 2015; Turner et al, 2015). The TROPOMI instrument scheduled for launch in 2017 will vastly expand the capability to observe methane from space by providing complete daily global coverage with 7×7 km^2 resolution (Veefkind et al., 2012; Butz et al., 2012). The GHGSat instrument launched on a microsatellite in June 2016 by the Canadian company GHGSat, Inc. has 50×50 m^2 pixel resolution over targeted viewing domains for detection of point sources. GOSAT-2, a successor of GOSAT featuring higher precision, is scheduled for launch in 2018. The MERLIN lidar instrument (Kiemle et al., 2011, 2014) is scheduled for launch in 2020. Additional instruments are in the planned or proposed stage. As the demand for global monitoring of methane emissions grows, it is timely to review the capabilities and limitations of present and future satellite observations.

2. Observing methane from space

2.1 Instruments and retrievals

Table 1 list the principal instruments (past, current, planned, proposed) measuring methane from space. Atmospheric methane is detectable by its absorption of radiation in the shortwave infrared (SWIR) at 1.65 and 2.3 μm, and in the thermal infrared (TIR) around 8 μm. Figure 2 shows different satellite instrument configurations. SWIR instruments measure solar radiation backscattered by the Earth and its atmosphere. The MERLIN lidar instrument will emit its own SWIR radiation and detect methane in the back-scattered laser signal. TIR instruments measure blackbody terrestrial radiation absorbed and re-emitted by the atmosphere. They can operate in the nadir as shown in Fig. 2, measuring upwelling radiation, or in the limb by measuring slantwise through the atmosphere. Solar occultation instruments (not shown in Fig. 2) stare at the Sun through the atmosphere as the orbiting satellite experiences sunrises and sunsets. Limb and solar occultation instruments detect methane in the stratosphere and upper troposphere, but not at lower altitudes because of cloud interferences. Thus they do not allow direct inference of methane emissions. They are not listed in Table 1 but are referenced in Sect. 3.2 for measuring stratospheric methane.

All instruments launched to date have been in polar sun-synchronous low Earth orbit (LEO), circling the globe at fixed local times of day. They detect methane in the nadir along the orbit track, and most also observe off-nadir (at a cross-track angle) for additional coverage. Unlike other instruments, GHGSat focuses not on global coverage but on specific targets with very fine pixel resolution and limited viewing domains. Geostationary instruments still at the proposal stage would allow a combination of high spatial and temporal resolution over continental-scale domains, and could observe either in the SWIR or in the TIR following the configurations of Fig. 2.

Figure 3 shows typical vertical sensitivities for solar back-scatter instruments in the SWIR and for thermal emission instruments in the TIR. Instrument sensitivity extending down to the surface is desirable to infer methane emissions. This is achieved in the SWIR, where the atmosphere is nearly transparent unless clouds are present (Frankenberg et al., 2005). SWIR instruments measure the total atmospheric column of methane with near-uniform sensitivity in the troposphere. This column measurement can be related to emissions in a manner that is not directly sensitive to local vertical mixing. Measurements in the TIR require a thermal difference between the atmosphere and the surface (T_1 vs. T_o in Fig. 2) and this limits their sensitivity to the middle and upper troposphere. Combination of SWIR and TIR could provide resolution of the lower troposphere but this has not been implemented operationally so far.

Figure 4 shows the atmospheric optical depths of different gases in the SWIR, highlighting the methane absorption bands at 1.65 µm and 2.3 µm. The data have been smoothed to 0.1 nm spectral resolution as is typical of solar backscatter instruments; lidar instruments such as MERLIN can operate with 0.1 pm resolution (Table 1). All solar backscatter instruments so far have operated at 1.65 µm but TROPOMI will operate at 2.3 µm. GOSAT-2 will operate at both. SCIAMACHY was intended to operate at 2.3 µm and some retrievals were done in that band (Gloudemans et al., 2008) but an ice layer on the detector decreased performance and the operational retrievals were done at 1.65 µm instead. The 2.3 µm band is stronger, as shown in Fig. 3, and also allows retrieval of carbon monoxide (CO) which is of interest as an air pollutant and tracer of transport (Worden et al., 2010). However, solar radiation is 3 times weaker at 2.3 than at 1.65 µm. The 1.65 µm band has the advantage that CO_2 can also be retrieved, which greatly facilitates the methane retrieval as described below.

Methane retrievals at either 1.65 or 2.3 µm fit the reflected solar spectrum measured by the satellite to a modeled spectrum in order to derive the total vertical column density Ω [molecules cm^{-2}] of methane, taking into account the viewing geometry and often including a prior estimate to regularize the retrieval (Frankenberg et al., 2006; Schepers et al., 2012):

$$\hat{\Omega} = \Omega_A + \mathbf{a}^T(\boldsymbol{\omega} - \boldsymbol{\omega}_A) \qquad (1)$$

Here $\hat{\Omega}$ is the retrieved vertical column density, Ω_A is the prior best estimate assumed in the retrieval, $\boldsymbol{\omega}_A$ is a vector of prior estimates of partial columns [molecules cm^{-2}] at successive altitudes summing up to Ω_A, and $\boldsymbol{\omega}$ is the vector of true values for these partial columns. The column averaging kernel vector **a** expresses the sensitivity of the measurement as a function of altitude (Fig. 3), and is the reduced expression of an averaging kernel matrix that describes the ability of the retrieval to fit not only $\boldsymbol{\omega}$ but other atmospheric and spectroscopic variables as well (Frankenberg et al., 2005; Schepers et al., 2012). The elements of **a** have values near unity through the depth of the troposphere at either 1.65 or 2.3 µm (Figure 3), meaning that SWIR instruments are sensitive to the full column of methane and that the prior estimates do not contribute significantly to the retrieved columns.

The viewing geometry of the satellite measurement is defined by the solar zenith angle θ and the satellite viewing angle θ_v (Fig. 2). This defines a geometric air mass factor ($\cos^{-1}\theta + \cos^{-1}\theta_v$) for the slant column path of the solar radiation propagating through the atmosphere and reflected to the satellite. Division by this air mass factor converts the slant column obtained by fitting the backscattered spectrum to the actual vertical column, assuming that the incident and reflected solar beams sample the same methane concentrations. This assumption is adequate for pixel sizes larger than 1 km but breaks down when observing methane plumes at smaller pixel sizes, as discussed in Sect. 4.

The methane vertical column density Ω is sensitive to changes in surface pressure from topography and weather, affecting the total amount of air in the column. This dependence can be removed by converting Ω to a dry-air column-average mole fraction $X = \Omega/\Omega_a$ (also called column-average mixing ratio) where Ω_a is the vertical column density of dry air as determined from the local surface pressure and humidity. X is a preferred measure of the methane concentration because it is insensitive to changes in pressure and humidity.

Solar backscatter measurements in the SWIR require a reflective surface. This largely limits the measurements to land, although some ocean data can be obtained from specular reflection at the ocean surface (sunglint). Clouds affect the retrieval by reflecting solar radiation back to space and preventing detection of the air below the cloud. Even partly cloudy scenes are problematic because the highly reflective cloudy fraction contributes disproportionately to the total backscattered radiation from the pixel. A major advantage of finer pixel resolution is thus to increase the probability of clear-sky scenes (Remer et al., 2012). The GOSAT retrievals exclude cloudy scenes by using a simultaneous retrieval of the oxygen column in the 0.76 μm *A*-band. A low oxygen column indicates the presence of cloud. For SCIAMACHY this is impractical because the pixel resolution is so coarse (30×60 km^2) that a clear-sky requirement would exclude too much data; instead the retrieval allows for partly cloudy scenes (Frankenberg et al., 2006). The fraction of successful retrievals is 17% for GOSAT (Parker et al. (2011) retrieval) and 9% for SCIAMACHY (Frankenberg et al. (2011) retrieval), largely limited by cloud cover. TROPOMI retrievals will exclude cloudy scenes by using cloud observations from the VIIRS solar backscatter instrument flying in formation and viewing the same scenes at fine pixel resolution (Veefkind et al., 2012).

Two different methods have been used for methane retrievals at 1.65 μm (SCIAMACHY, GOSAT): the CO_2 proxy method (Frankenberg et al., 2005) and the full-physics method (Butz et al., 2010). In the full-physics method, the scattering properties of the surface and the atmosphere are fitted as part of the retrieval, using additional fitting variables to describe the scattering. In the CO_2 proxy method, the spectral fit for methane ignores atmospheric scattering, and the resulting methane column is subsequently corrected for scattering by using a separate retrieval of CO_2 (also ignoring atmospheric scattering) in its nearby 1.6 μm absorption band as shown in Fig. 4. This assumes that atmospheric scattering affects the light paths for methane and CO_2 retrievals in the same way (since the wavelengths are nearby and absorption strengths are similar). It also assumes that the dry-air column mole fraction of CO_2 is known (it is far less variable than for methane). The dry-air column mole fraction of methane is then obtained by scaling to the CO_2 retrieval:

$$X_{CH4} = \left(\frac{\Omega_{CH4}}{\Omega_{CO2}}\right) X_{CO2} \tag{2}$$

Here X_{CO2} is taken from independent information such as the CarbonTracker data assimilation product (Peters et al., 2007) or a multi-model ensemble (Parker et al., 2015). An advantage of the CO_2 proxy method is that it corrects for instrument biases affecting both methane and CO_2. A drawback is that errors in X_{CO2} propagate to X_{CH4}. Comparisons of retrievals using the full-physics and CO_2 proxy methods show that they are of comparable quality (Buchwitz et al., 2015) but the CO_2 proxy method is much more computationally efficient (Schepers et al., 2012). The CO_2 proxy method can be problematic for methane plumes with joint enhancements of CO_2, such as from megacities or open fires, that would not be resolved in the independent information for X_{CO2}. Uncertainties in X_{CO2} can be circumvented by using the X_{CH4}/X_{CO2} ratio as observed variable in a joint inversion of methane and CO_2 surface fluxes (Fraser et al., 2014; Pandey et al., 2015).

Figure 5 shows the global and US distributions of methane (X_{CH4}) observed by SCIAMACHY (2003-2004) and GOSAT (2010-2013). We focus on 2003-2004 for SCIAMACHY because of radiation-induced detector degradation after 2005 (Kleipool et al., 2007). Global methane concentrations increased by 30 ppb from 2003-2004 to 2010-2013 (Hartmann et al., 2013), and the colorscale in Fig. 5 is correspondingly shifted to facilitate pattern comparisons. Observations are mainly restricted to land but GOSAT also observes sunglint over the oceans. SCIAMACHY provides full global mapping, while GOSAT observes only at selected pixel locations leaving gaps between pixels. Low values of X_{CH4} over elevated terrain (Greenland, Himalayas, US Intermountain West) reflect a larger relative contribution of the stratosphere (with lower methane) to the total atmospheric column. SCIAMACHY has positive biases over the Sahara and at high latitudes (Sect. 2.2).

The SCIAMACHY and GOSAT global distributions show commonality in patterns. Values are highest in East Asia, consistent with the Emissions Database for Global Atmospheric Research (EDGAR) inventory (European Commission, 2011), where the dominant contributions are from rice cultivation, livestock, and coal mining. Values are also high over central Africa and northern South America because of wetlands and livestock. Over the US, both SCIAMACHY and GOSAT feature high values in the South-Central US (oil/gas, livestock) and hotspots in the Central Valley of California and in eastern North Carolina (livestock). There are also high values in the Midwest that are less consistent between the two sensors and could be due to a combination of oil/gas, livestock, and coal mining sources.

TROPOMI will observe methane in the 2.3 μm band in order to also retrieve CO. Retrieval at 2.3 μm does not allow the CO_2 proxy method because no neighboring CO_2 band is available (Fig. 4). Retrievals of methane from TROPOMI will therefore rely on the full-physics method. The operational retrieval for TROPOMI is described by Butz et al. (2012), who find that the precision error is almost always better than 1% and that over 90% of cloud-free scenes can be successfully retrieved. Observations of methane-CO correlations from joint 2.3 μm retrievals may provide useful additional information for inferring methane sources (Xiao et al., 2004; Wang et al., 2009; Worden et al., 2013).

Observations of methane in the TIR are available from the IMG, AIRS, TES, IASI, and CrIS instruments (Table 1). These instruments observe the temperature-dependent blackbody radiation emitted by the Earth and its atmosphere. Atmospheric methane absorbs upwelling radiation in a number of bands around 8 μm and re-emits it at a colder temperature. The methane concentration is retrieved from the temperature contrast. TIR instruments have little sensitivity to the lower troposphere because of insufficient temperature contrast with the surface, as illustrated in Fig. 3. This makes them less useful for detecting local/regional methane emissions. On the other hand, they observe both day and night, over land and ocean, and provide concurrent retrievals of other trace gases such as CO and ammonia that can be correlated with methane. Worden et al. (2013) showed that TIR measurements can be particularly effective at quantifying methane emissions from open fires, because aerosol interference is negligible in the TIR and concurrent retrieval of CO allows inference of the methane/CO emission factor.

Multispectral retrievals in the SWIR and TIR combine the advantages of both approaches and provide some vertical profile information, as demonstrated by Herbin et al. (2013) using the combination of SWIR and TIR data from GOSAT, and by Worden et al. (2015) using the combination of SWIR from GOSAT and TIR from TES. This could enable separation between the local/regional methane enhancement near the surface and the higher-altitude methane background (Bousserez et al., 2015). Such multi-spectral retrievals are not yet produced operationally because of computational requirements and because of limitations in the quality and calibration of spectra across different detectors (Hervé Herbin, personal communication).

The MERLIN lidar instrument scheduled for launch in 2020 (Kiemle et al., 2011) will measure methane in the pencil of 1.65 μm radiation emitted by a laser along the satellite track and reflected directly back to the satellite. It will observe the full vertical column of methane during day and night, over both land and oceans, and will have unique capability for observing high latitudes during the dark season. By measuring only the direct reflected radiation it will not be affected by scattering errors, unlike the passive SWIR instruments, and cloud interferences willl be minimized. Kiemle et al. (2014) show that monthly and spatial averaging of the MERLIN data on a 50×50 km^2 grid should provide global mapping of methane concentrations with 1-2% precision.

Other instruments in Table 1 are presently at the proposal stage. All use solar backscatter. CarbonSat (Buchwitz et al., 2013) is designed to measure methane globally with an unprecedented combination of fine pixel resolution (2×2 km^2) and high precision (0.4%). It was a finalist for the ESA's Earth Explorer Program in 2015. GEO-CAPE (Fishman et al., 2012), GeoFTS (Xi et al., 2015), geoCARB (Polonsky et al., 2014), and G3E (Butz et al., 2015) are geostationary instruments focused on mapping the continental scale with 2-5 km resolution. focus. Geostationary capabilities are discussed further in Sect. 4.

2.2 Error characterization

Satellite observations require careful calibration and error characterization for use in inverse analyses. Errors may arise from light collection by the instrument, dark current, spectroscopic data, the radiative transfer model, cloud contamination, and other factors. Kuze et al. (2016) give a detailed description of GOSAT instrument errors as informed by 5 years of operation. Errors may be random, such as from photon count statistics, or systematic, such as from inaccurate spectroscopic data. They may increase with time due to instrument degradation.

Random error (precision) and systematic error (accuracy) have very different impacts (Kulawik et al., 2016). Random error can be reduced by repeated observations and averaging. As we will illustrate in Sect. 4, instrument precision can define the extent of spatial/temporal averaging required for satellite observations to usefully quantify emissions. Systematic error, on the other hand, is irreducible and propagates in the inversion to cause a corresponding bias in the emission estimates. A uniform global bias is not problematic for methane since the global mean concentration is well known from surface observations, but a spatially variable bias affects source attribution by aliasing the methane enhancements relative to background. Buchwitz et al. (2015) refer to this spatial variability in the bias as "relative bias". It can arise for example from different surface reflectivities, aerosol interference, sloping terrain, or unresolved variability in CO_2 columns when using the CO_2 proxy method (Schepers et al., 2012; Alexe et al., 2015). Buchwitz et al. (2015) estimate threshold requirements of 34 ppb single-observation precision and 10 ppb relative bias for solar backscatter satellite observations to be useful in inversions of methane emissions on regional scales.

Validation of satellite data requires accurate suborbital observations of methane from surface sites, aircraft, or balloons. Direct validation involves comparison of single-scene satellite retrievals to suborbital observations of that same scene. The suborbital observations must be collocated in space and time with the satellite overpass, and they must provide a full characterization of the column as observed by the satellite. Although direct validation is the preferred means of validation, the requirements greatly limit the conditions under which it can be done. Indirect validation is a complementary method that involves diagnosing the consistency between satellite and suborbital data when compared to a global 3-D CTM as a common intercomparison platform (Zhang et al., 2010). It considerably increases the range of suborbital measurements that can be used because collocation in space and time is not required. Indirect validation can also be conducted formally by chemical data assimilation of the different observational data streams into the CTM.

The standard benchmark for direct validation of solar backscatter satellite observations is the worldwide Total Carbon Column Observing Network (TCCON) (Wunch et al., 2011). TCCON consists of ground-based Fourier Transform Spectrometer (FTS) instruments staring at the Sun and detecting methane absorption in the direct solar radiation spectrum. This measures the same dry-air column mole fraction X_{CH4} as the satellite but with much better signal-to-noise and a well-defined light path. The TCCON retrieval of methane is calibrated to the World Meteorological Organization (WMO) scale and has been validated by comparison to aircraft profiles (Wunch et al., 2011). The single-observation precision and bias for X_{CH4} are both about 4 ppb (Buchwitz et al., 2015).

Dils et al. (2014) and Buchwitz et al. (2015) present direct validation of the different operational SCIAMACHY and GOSAT retrievals using TCCON data. Relative bias is determined using pairs of TCCON sites. They find a single-observation precision of 30 ppb and relative bias of 4-13 ppb for SCIAMACHY in 2003-2005, good enough for inverse applications, but worsening after 2005 to 50-82 ppb (precision) and 15 ppb (relative bias). For GOSAT, they report single-observation precisions of 12-13 ppb for the CO_2 proxy products and 15-16 ppb for the full-physics products. Relative biases for GOSAT are 2-3 ppb for the CO_2 proxy products and 3-8 ppb for the full-physics products. Thus the GOSAT data are of high quality for use in inversions. The CO_2 proxy retrievals provide a much higher density of observations than the full-physics retrievals, so that random errors can be effectively decreased and the precision improved through temporal averaging.

TIR measurements are most sensitive to the middle/upper troposphere (Fig. 3) and aircraft vertical profiles provide the best resource for direct validation. Wecht et al. (2012) and Alvarado et al. (2015) evaluated successive versions of TES methane retrievals with data from the HIPPO pole-to-pole aircraft campaigns over the Pacific (Wofsy, 2011). Alvarado et al. (2015) report that the latest Version 6 of the TES product has a bias of 4.8 ppb. Crevoisier et al. (2011) find that IASI observations are consistent with aircraft observations to within 5 ppb.

Use of satellite observations in inverse modeling studies cannot simply rely on past validation to quantify the instrument error. This is because the instrument calibration may drift with time, optics and detectors may degrade, and errors may vary depending on surface and atmospheric conditions. It is essential that error characterization be done for the specific temporal and spatial window of the inversion. Opportunities for direct validation may be sparse but indirect validation with the CTM to be used for the inversion is particularly effective. Such indirect validation can exploit all relevant suborbital data collected in the window to assess their consistency with the satellite data. This has been standard practice in inversions of SCIAMACHY and GOSAT data, and has resulted in correction factors applied to the data as a function of latitude (Bergamaschi et al., 2009, 2013; Fraser et al., 2013; Alexe et al., 2015;

Turner et al., 2015), water vapor (Houweling et al., 2014; Wecht et al., 2014a), or air mass factor (Cressot et al., 2014).

3. Inferring methane emissions from satellite data

3.1 Overview of inverse methods

The general approach for inferring methane emissions from observed atmospheric concentrations is to use a 3-D CTM describing the sensitivity of concentrations to emissions. The CTM simulates atmospheric transport on the basis of assimilated meteorological data for the observation period and a 2-D field of gridded emissions. It computes concentrations as a function of emissions by solving the mass continuity equation that describes the change in the 3-D concentration field resulting from emissions, winds, turbulence, and chemical loss. In Eulerian CTMs, the solution to the continuity equation is done on a fixed atmospheric grid. In Lagrangian CTMs, often called Lagrangian Particle Dispersion Models (LPDMs), the solution is obtained by tracking a collection of air particles moving with the flow. Eulerian models have the advantage of providing a complete, continuous, and mass-conserving representation of the atmosphere. LPDMs have the advantage of being directly integrable backward in time, so that the source footprint contributing to the concentrations at a particular receptor point is economically computed. Eulerian models can also be integrated backward in time to derive source footprints by using the model adjoint (Henze et al., 2007). LPDMs have been used extensively for inverse analyses of ground and aircraft methane observations, where the limited number of receptor points makes the Lagrangian approach very efficient (Miller et al., 2013; Ganesan et al., 2015; Henne et al., 2016). Satellite observations involve a considerably larger number of receptor points, including different altitudes contributing to the column measurement. For this reason, all published inversions of satellite methane data so far have used Eulerian CTMs. A preliminary study by Benmergui et al. (2015) applies an LPDM to inversion of GOSAT data.

The CTM provides the sensitivity of concentrations to emissions at previous times. By combining this information with observed concentrations we can solve for the emissions needed to explain the observations. Because of errors in measurements and in model transport, the best that can be achieved is an error-weighted statistical fit of emissions to the observations. This must account for prior knowledge of the distribution of emissions, generally from a bottom-up inventory, in order to target the fit to the most relevant emission variables and in order to achieve an optimal estimate of emissions consistent with all information at hand.

The standard method for achieving such a fit is Bayesian optimization. The emissions are assembled into a state vector $\mathbf{x}$ (dim n), and the observations are assembled into an observation vector $\mathbf{y}$ (dim m). Bayes' theorem gives

$$P(\mathbf{x} \mid \mathbf{y}) = \frac{P(\mathbf{x})P(\mathbf{y} \mid \mathbf{x})}{P(\mathbf{y})} \qquad (3)$$

where $P(\mathbf{x})$ and $P(\mathbf{y})$ are the probability density functions (PDFs) of $\mathbf{x}$ and $\mathbf{y}$, $P(\mathbf{x}|\mathbf{y})$ is the conditional PDF of $\mathbf{x}$ given $\mathbf{y}$, and $P(\mathbf{y}|\mathbf{x})$ is the conditional PDF of $\mathbf{y}$ given $\mathbf{x}$. We recognize here $P(\mathbf{x})$ as the prior PDF of $\mathbf{x}$ before the observations $\mathbf{y}$ have been made, $P(\mathbf{y}|\mathbf{x})$ as the observation PDF given the true value of $\mathbf{x}$ (for which the observations were made), and $P(\mathbf{x}|\mathbf{y})$ as the posterior PDF of **x** after the observations **y** have been made. The optimal estimate of emissions is defined by the maximum of $P(\mathbf{x}|\mathbf{y})$, which we obtain by solving $\nabla_{\mathbf{x}} P(\mathbf{x}\,|\,\mathbf{y}) = \mathbf{0}$.

In the absence of better information, error PDFs are often assumed to be Gaussian (Rodgers, 2000). We then have

$$P(\mathbf{x}) = \frac{1}{(2\pi)^{n/2}\left|\mathbf{S_A}\right|^{1/2}} \exp[-\frac{1}{2}(\mathbf{x} - \mathbf{x_A})^T \mathbf{S_A}^{-1}(\mathbf{x} - \mathbf{x_A})] \quad (4)$$

$$P(\mathbf{y}\,|\,\mathbf{x}) = \frac{1}{(2\pi)^{m/2}\left|\mathbf{S_O}\right|^{1/2}} \exp[-\frac{1}{2}(\mathbf{y} - \mathbf{F(x)})^T \mathbf{S_O}^{-1}(\mathbf{y} - \mathbf{F(x)})] \quad (5)$$

where $\mathbf{x_A}$ is the prior estimate, $\mathbf{S_A}$ is the associated prior error covariance matrix, **F** is the CTM solving for **y** = **F**(**x**) and is called the forward model for the inversion, and $\mathbf{S_O}$ is the observational error covariance matrix including contributions from measurement and CTM errors. An important assumption here is that the observational error is random; any known systematic bias in the measurement or the CTM must be corrected before the inversion is conducted. This requires careful validation (Sect. 2.2).

The optimization problem $\nabla_{\mathbf{x}} P(\mathbf{x}\,|\,\mathbf{y}) = \mathbf{0}$ is solved by minimizing the cost function $J(\mathbf{x})$:

$$J(\mathbf{x}) = (\mathbf{x} - \mathbf{x_A})^T \mathbf{S}_\mathbf{A}^{-1}(\mathbf{x} - \mathbf{x_A}) + (\mathbf{y} - \mathbf{F(x)})^T \mathbf{S}_\mathbf{O}^{-1}(\mathbf{y} - \mathbf{F(x)}) \quad (6)$$

where the PDFs have been converted to their logarithms and the terms independent of **x** have been discarded. In particular, $P(\mathbf{y})$ in Eq. (3) is discarded since it does not depend on **x**. The minimum of J is found by differentiating Eq. (6):

$$\nabla_{\mathbf{x}} J(\mathbf{x}) = 2\mathbf{S}_\mathbf{A}^{-1}(\mathbf{x} - \mathbf{x_A}) + 2\mathbf{K}^T \mathbf{S}_\mathbf{O}^{-1}(\mathbf{F}(\mathbf{x}) - \mathbf{y}) = \mathbf{0} \quad (7)$$

where $\mathbf{K} = \nabla_{\mathbf{x}}\mathbf{F} = \partial\mathbf{y}/\partial\mathbf{x}$ is the Jacobian of **F** and $\mathbf{K}^T$ is its adjoint.

Analytical method. Equation (7) can be solved analytically if the relationship between emissions and atmospheric concentrations is linear, such that **F(x) = Kx + c** where **c** is a constant. This is the case for methane if the tropospheric OH concentration field used in the CTM to compute methane loss is not affected by changes in methane. Although methane and OH levels are interdependent because methane is a major OH sink (Prather, 1996), the global methane loading relevant for computing OH concentrations is well known (Prather et al., 2012). It is therefore totally appropriate to treat OH concentrations as decoupled from methane in the inversion. Analytical solution of Eq. (7) for a linear model **y** = **F(x)** (where the constant **c** can be simply subtracted from the observations) yields an optimal estimate $\hat{\mathbf{x}}$ with Gaussian error characterized by an error covariance matrix $\hat{\mathbf{S}}$ (Rodgers, 2000):

$$\hat{\mathbf{x}} = \mathbf{x_A} + \mathbf{G}(\mathbf{y} - \mathbf{K}\mathbf{x_A}) \quad (8)$$

$$\hat{\mathbf{S}} = (\mathbf{K}^T \mathbf{S}_\mathbf{O}^{-1} \mathbf{K} + \mathbf{S}_\mathbf{A}^{-1})^{-1} \tag{9}$$

Here **G** is the gain matrix given by

$$\mathbf{G} = \mathbf{S_A} \mathbf{K}^T (\mathbf{K} \mathbf{S_A} \mathbf{K}^T + \mathbf{S_O})^{-1} \tag{10}$$

The degree to which the observations constrain the state vector of emissions is diagnosed by the averaging kernel matrix $\mathbf{A} = \partial \hat{\mathbf{x}} / \partial \mathbf{x} = \mathbf{GK} = \mathbf{I_n} - \hat{\mathbf{S}} \mathbf{S}_\mathbf{A}^{-1}$ expressing the sensitivity of the optimized estimate to the actual emissions **x**. Here $\mathbf{I_n}$ is the $n \times n$ identity matrix. The observations may adequately constrain some features of the emission field and not others. The number of independent pieces of information on the emission field provided by the observing system is given by the trace of **A** and is called the degrees of freedom for signal (DOFS = tr(**A**)).

Analytical solution to the inverse problem provides full error characterization of the solution through $\hat{\mathbf{S}}$ and **A**. This is a very attractive feature, particularly for an underconstrained problem where we need to understand what information the observations actually provide. However, it requires explicit construction of the Jacobian matrix. With an Eulerian CTM this requires *n* individual simulations, each providing a column *j* of the Jacobian $\partial \mathbf{y} / \partial x_j$. With an LPDM (or the adjoint of an Eulerian CTM), this requires *m* individual simulations tracking the backward transport from a given observation location and providing a row *i* of the Jacobian $\partial y_i / \partial \mathbf{x}$. Either way is a computational challenge when using a very large number *m* of satellite observations to optimize a very large number *n* of emission elements with high resolution.

Equations (8)-(10) further require the multiplication and inversion of large matrices of dimensions *m* and *n*. This curse of dimensionality can be alleviated by ingesting the observations sequentially as uncorrelated data packets (thus effectively reducing *m*) (Rodgers, 2000) and by recognizing that individual state vector elements have only a limited zone of influence on the observations (thus effectively reducing *n* or taking advantage of sparse-matrix methods) (Bui-Thanh et al., 2012). When observations are ingested sequentially for successive time periods with each packet used to update emissions for the corresponding period we refer to the method as a Kalman filter.

There is danger in over-interpreting the posterior error covariance matrix $\hat{\mathbf{S}}$ when the number of observations is very large, as from a satellite data set, because of the implicit assumption that observational errors are truly random and are representatively sampled over the PDF. CTM errors are rarely unbiased and generally not representatively sampled. Thus $\hat{\mathbf{S}}$ tends to be an over-optimistic characterization of the error on the optimal estimate. An alternate approach for error characterization is to compute an ensemble of solutions with modified prior estimates, forward model, inverse methods, or error estimates (Heald et al., 2004; Henne et al., 2016).

Adjoint method. The limitation on the size of the emission state vector can be lifted by solving equation (7) numerically instead of analytically. This is done by applying iteratively the adjoint of the CTM, which is the model operator $\mathbf{K}^T$, to the error-weighted model-observation differences $\mathbf{S}_\mathbf{O}^{-1}(\mathbf{F}(\mathbf{x}) - \mathbf{y})$. We discussed above how this backward transport provides the sensitivity of concentrations to emissions at prior times, i.e., the footprint of the concentrations.

Here we apply it to determine the footprint of the errors in emissions as diagnosed by the model-observation differences. For an Eulerian CTM the adjoint must be independently constructed (Henze et al., 2007), while for a LPDM it is simply obtained by transporting the air particles backward in time.

The iterative procedure in the adjoint method is as follows. Starting from the prior estimate $\mathbf{x_A}$ as initial guess, we apply the adjoint operator $\mathbf{K}^T$ to the error-weighted model-observation differences $\mathbf{S_O^{-1}}(\mathbf{F}(\mathbf{x_A})-\mathbf{y})$ and in this manner determine the sensitivity of these differences to emissions earlier in time; this defines the cost function gradient $\nabla_{\mathbf{x}} J(\mathbf{x_A})$ in equation (7). By applying $\nabla_{\mathbf{x}} J(\mathbf{x_A})$ to $\mathbf{x_A}$ with a steepest-descent algorithm we obtain a next guess $\mathbf{x_1}$ for the minimum of $J(\mathbf{x})$, compute the corresponding vector $\mathbf{K}^T\mathbf{S_O^{-1}}(\mathbf{F}(\mathbf{x_1})-\mathbf{y})$, and add the error-weighted difference from the prior estimate $\mathbf{S_A^{-1}}(\mathbf{x_1}-\mathbf{x_A})$ to obtain the cost function gradient $\nabla_{\mathbf{x}} J(\mathbf{x_1})$. By applying $\nabla_{\mathbf{x}} J(\mathbf{x_1})$ to $\mathbf{x_1}$ with the steepest-descent algorithm we obtain a next guess $\mathbf{x_2}$, and iterate in this manner to find the minimum of $J(\mathbf{x})$ (Henze et al. 2007). A major advantage of the adjoint method is that the Jacobian is never explicitly computed, and there are no multiplication/inversion operations involving large matrices. Thus there is no computational limitation on the dimension of **x.** Another major advantage is that the error PDFs do not need to be Gaussian. A drawback is that error characterization is not included as part of the solution. Approximate methods are available at additional computational cost to estimate the posterior error covariance matrix $\hat{\mathbf{S}}$ and from there the averaging kernel matrix **A** (Bousserez et al., 2015).

MCMC methods. Markov Chain Monte Carlo (MCMC) methods are yet another approach to solve the Bayesian inverse problem. Here the posterior PDF $P(\mathbf{x}|\mathbf{y})$ is constructed by direct computation from equation (3) using stochastic sampling of the **x** domain and with any chosen forms for $P(\mathbf{x})$ and $P(\mathbf{y}|\mathbf{x})$. Starting from the prior estimate $\mathbf{x_A}$, we compute $P(\mathbf{x_A})$ and $P(\mathbf{y}|\mathbf{x_A})$, and from there compute $P(\mathbf{x_A}|\mathbf{y})$ using Eq. (3). We then define the next element of the Markov chain as $\mathbf{x}_1 = \mathbf{x_A} + \Delta\mathbf{x}$, where $\Delta\mathbf{x}$ is a random increment, compute $P(\mathbf{x}_1|\mathbf{y})$, and so on. With a suitable algorithm to sample representatively the **x** domain as successive elements of the Markov chain, the full structure of $P(\mathbf{x}|\mathbf{y})$ is eventually constructed. Miller et al. (2014) and Ganesan et al. (2015) used MCMC methods in regional inversions of suborbital methane data. A major advantage is that the prior and observation PDFs can be of any form. For example, the prior PDF can include a "fat tail" to allow for the possibility of a point source behaving as a "super-emitter" either continuously or sporadically (Zavala-Araiza et al., 2015). Another advantage is that the full posterior PDF of the solution is obtained (not just the optimal estimate). The main drawback is the computational cost of exploring the *n*-dimensional space defined by **x**.

There are other ways of expressing the prior information than as $(\mathbf{x_A}, \mathbf{S_A})$. In the hierarchical Bayesian approach (Ganesan et al., 2014), information on the prior is optimized as part of the inversion. In the geostatistical approach (Michalak et al., 2006), prior information is expressed in terms of emission patterns rather than magnitudes. The cost function in the geostatistical inversion is

$$J(\mathbf{x},\boldsymbol{\beta}) = (\mathbf{x}-\mathbf{P}\boldsymbol{\beta})^T\mathbf{S}^{-1}(\mathbf{x}-\mathbf{P}\boldsymbol{\beta}) + (\mathbf{y}-\mathbf{F}(\mathbf{x}))^T\mathbf{S_O^{-1}}(\mathbf{y}-\mathbf{F}(\mathbf{x})) \quad (11)$$

where the $n \times q$ matrix **P** describes the q different state vector patterns, with each column of **P** describing a normalized pattern such as the distribution of livestock. The unknown vector $\boldsymbol{\beta}$ of dimension q gives the mean scaling factor for each pattern. Thus $\mathbf{P}\boldsymbol{\beta}$ represents a prior model for the mean, with $\boldsymbol{\beta}$ to be optimized as part of the inversion. The covariance matrix **S** gives the prior covariance of **x**, rather than the error covariance.

Inverse methods for constraining emissions can be applied not only to current observing systems but also to evaluate formally the capability of a proposed future instrument to improve current knowledge. Given an observation plan and error specifications for the proposed instrument, we can compute the expected observational error covariance matrix $\mathbf{S_O}$. Given the prior information ($\mathbf{x_A}, \mathbf{S_A}$) informed by the current observing system without the proposed instrument, we can quantify the information added by the proposed instrument by computing $\hat{\mathbf{S}}$ from Eq. (9) or an adjoint-based approximation (Bousserez et al., 2015). From there we obtain the averaging kernel matrix $\mathbf{A} = \mathbf{I_n} - \hat{\mathbf{S}}\mathbf{S}_\mathbf{A}^{-1}$ and the DOFS, and compare to the DOFS without the instrument to quantify the information to be gained. This assessment will tend to be optimistic because of the assumption that errors are random, well characterized, and representatively sampled, as discussed above. But at least it demonstrates the potential of the proposed instrument. Applications to methane are presented in Sect. 3.4.

The simple error analysis described above to assess the value of a future instrument is sometimes loosely called an observing system simulation experiment (OSSE). However, the OSSE terminology is generally reserved for a more rigorous test (and an actual 'experiment') of the benefit of adding the proposed instrument to the current observing system, including realistic accounting of CTM errors. A standard OSSE setup is illustrated in Figure 6. The OSSE uses two CTMs driven by different assimilated meteorological datasets for the same period. The first model (CTM1) produces a synthetic 3-D field of atmospheric concentrations from an emission inventory taken as the "true" emissions (A in Fig. 6). For purpose of the exercise, CTM1 is taken to have no error and so describes the "true" 3-D field of atmospheric concentrations. This "true" atmosphere is then sampled synthetically with the current observing system, adding instrument noise as stochastic random error, so that the resulting synthetic data mimic the current observing system. Inversion of these data returns emissions optimized by the current observing system (B in Fig. 6) We then add the proposed instrument to the observing system, again adding instrument noise as random error on the basis of the instrument specifications, and invert the data using the previously optimized emissions (B) as prior estimate. The resulting optimized emissions (C in Fig. 6) can be compared to the "true" emissions (A) and to the prior emissions (B) to quantify the value of the proposed instrument and its advantage relative to the current observing system. The use of two independent assimilated meteorological data sets is important for this exercise as it allows for realistic accounting of the CTM error component. Such an OSSE setup is frequently used to evaluate proposed meteorological instruments, and it has previously been applied to the evaluation of a geostationary instrument for tropospheric ozone (Zoogman et al., 2014) but not so far for methane.

3.2 Specific issues in applying inverse methods to satellite methane data

There are a number of issues requiring care in the application of inverse methods to infer methane emissions from observations of atmospheric methane, some of which are specific to satellite observations.

Selection of emission state vector. A first issue relates to the resolution of the emission field (state vector) to be optimized by the inversion. Methane originates from a large number of scattered sources, with emission factors that are poorly known and highly variable for a given source sector. It is therefore of interest to optimize emissions with fine spatial resolution, and for some sources also with fine temporal resolution. The resolution of the emission state vector can in principle be as fine as the grid resolution and time step of the CTM used as forward model. However, the amount of information contained in the observations places limits on the extent to which emissions can actually be resolved. Satellite data sets may be large but the data are noisy. If the dimension of the emission state vector is too large relative to the information content of the observations, then the Bayesian optimization problem is underconstrained and the solution may be heavily weighted by the prior estimate. This is known as the smoothing error and the associated error covariance matrix is $(\mathbf{I_n} - \mathbf{A})\mathbf{S_A}(\mathbf{I_n} - \mathbf{A})^T$ (Rodgers, 2000). Smoothing is not a problem *per se* if the off-diagonal structure of $\mathbf{S_A}$ is well-characterized, so that information can propagate between state vector elements; but it generally is not. When $\mathbf{S_A}$ is specified diagonal, as is often the case, the ability to depart from the prior estimate and reduce the posterior error will be artificially suppressed if the dimension of $\mathbf{x}$ is too large (Wecht et al., 2014a).

Figure 7 illustrates the smoothing problem in an inversion of methane emissions over North America using SCIAMACHY. The cure is to reduce the dimension of the emission state vector, by aggregating state vector elements and optimizing only the aggregate (Fig. 7). This introduces however another type of error, known as aggregation error, because the relationship between aggregated state vector elements is now imposed by the prior estimate (Kaminski et al., 2001). As shown by Turner and Jacob (2015) and illustrated in Fig. 7, it is possible to define an optimal dimension of the emission state vector by balancing the smoothing and aggregation errors. For a multi-annual GOSAT data set this implies a spatial resolution of the order of 100-1000 km in methane source regions (Turner et al., 2015). The state vector of emissions can be reduced optimally by hierarchical clustering (Wecht et al., 2014a) or by using radial basis functions with Gaussian PDFs (Turner and Jacob, 2015).

Bottom-up inventory used as prior estimate. Inverse analyses require high-quality gridded bottom-up inventories as prior estimates to regularize the solution and interpret results. All inversions of methane satellite data so far have relied on the EDGAR bottom-up inventory for anthropogenic emissions with $0.1^o \times 0.1^o$ spatial resolution (European Commission, 2011), which is presently the only global bottom-up inventory available on a fine grid. EDGAR relies on IPCC (2006) default tier 1 methods that are relatively crude and it provides only limited classification of methane emissions by source sector. Alexe et al. (2015) and Turner et al. (2015) find that uncertainties in source patterns in the EDGAR inventory preclude the attribution of inventory corrections from their GOSAT inversions to specific source sectors. Many individual countries produce national inventories using more accurate IPCC tier 2/3 methods but these inventories are generally available only as national totals and are thus not usable for inversions, where information on spatial pattterns is essential.

The need for improved, finely gridded bottom-up inventories for inverse analyses is well recognized. Wang and Bentley (2002) disaggregated the Australian national inventory to guide inversion of surface observations at Cape Grim, Tasmania. Zhao et al. (2009) disaggregated the California Air Resources Board (CARB) statewide inventory to a $0.1^o \times 0.1^o$ grid. Hiller et al. (2014) disaggregated the Swiss national inventory to a 500×500 m^2 grid. Maasakkers et al. (2016) developed a gridded $0.1^o \times 0.1^o$ version of the national US emission inventory produced by

EPA (Fig. 1) and shows major differences with EDGAR in terms of source patterns even though the national totals are similar.

Positivity of the solution. The standard assumption of Gaussian error PDFs for the prior estimate allows for the possibility of negative methane emissions. Although soils can be a weak sink for methane (Kirschke et al., 2013), negative emissions are generally unphysical. Small negative values may be acceptable as noise, and can be removed by averaging with neighboring positive values. The analytical solution to the Bayesian inverse problem requires Gaussian error PDFs (Sect. 3.1), but numerical solutions do not. Adjoint-based inversions may use lognormal (Wecht et al., 2014a) or semi-exponential (Bergamaschi et al., 2013) error distributions to prevent negative solutions. Lognormal errors can be used in the analytical solution by adopting as state vector the logarithm of emissions but this requires iterative recomputation of the Jacobian matrix since the relation between state vector **x** and observations **y** is not linear anymore. Miller et al. (2014) present additional approaches for imposing positivity of the solution, including (1) application of Karush-Kuhn-Tucker (KKT) conditions, and (2) MCMC methods with sampling domain restriction. These approaches will tend to bias the solution by enforcing zero values for a subset of the state vector (KKT conditions) or by artificially inflating the PDF of the prior estimate in the vicinity of zero (MCMC methods).

Variability in the methane background. Observations from the HIPPO pole-to-pole aircraft campaigns over the Pacific in 2010-2011 indicate background concentrations of tropospheric methane varying with latitude from 1750-1800 ppb in the southern hemisphere to 1850-1900 ppb at high northern latitudes (Wofsy, 2011). The mid-latitudes background varies on synoptic scales under the alternating influence of high-latitude and low-latitude air masses. This variability in background is comparable to the magnitude of concentration enhancements in methane source regions, so that accurate accounting of the global methane background and its variability is essential for regional inversions. Local source inversions may be able to use instead regional background information upwind of the source (Krings et al., 2013).

Observations at remote sites from the NOAA Earth System Research Laboratory (ESRL) network (Dlugokencky et al., 2011; Andrews et al., 2014) accurately characterize the seasonal latitude-dependent background, and one can then rely on the CTM used as forward model in the inversion to resolve the synoptic variations in that background. Global inversions of satellite data have exploited the NOAA ESRL network data in different ways. Bergamaschi et al. (2009, 2013), Fraser et al. (2013), and Alexe et al. (2015) included the data in their inversions together with the satellite data. Cressot et al (2014) conducted separate inversions with NOAA/ESRL and satellite data, and demonstrated consistency between the two. In limited-domain inversions such as on the continental scale of North America, the background must be specified as a time- and latitude-dependent boundary condition. This has been done by Miller et al. (2013) using the NOAA/ESRL data as boundary conditions, in Wecht et al. (2014a) by optimizing the boundary conditions as part of the inversion, and by Turner et al. (2015) by using results from a global inversion as boundary conditions for the continental-scale inversion.

Methane sink in the troposphere. The main sink for methane is oxidation by the OH radical in the troposphere, with a lifetime of 9 years constrained by global observations of methylchloroform (MCF) (Prather et al., 2012). OH is produced photochemically and its concentration is controlled by complex chemistry that is not well represented in models

(Voulgarakis et al., 2013). However, the loss of methane is sufficiently slow that variability in OH concentrations affects methane concentrations only on seasonal, interannual, and interhemispheric scales (Bousquet et al., 2006). It does not affect the regional-scale gradients relevant to inverse analyses of satellite data. Global inverse analyses generally compute the methane sink by using specified global 3-D monthly fields of OH concentrations from an independent simulation of tropospheric oxidant chemistry and compatible with the MCF constraint (Bergamaschi et al, 2013; Houweling et al., 2014). Cressot et al. (2014) optimized methane and MCF emissions together in their inversion, thus allowing for adjustment of OH concentrations within the uncertainty range allowed by MCF. Specifying OH concentrations is not an issue for limited-domain inversions with spatial boundary conditions, because the modeling domain is then ventilated on a time scale considerably shorter than the 9-year methane lifetime. In that case, information on the methane sink is effectively incorporated in the boundary conditions.

Stratospheric methane. Inversions of satellite methane data require a proper accounting of the stratosphere. The stratosphere contributes about 5% of the total methane column in the tropics and 25% at high latitudes (Ostler et al., 2015). Methane enters the stratosphere in the tropics and is transported to high latitudes on a time scale of about 5 years. Over that time it is photochemically oxidized by OH, $O(^1D)$, and Cl atoms, leading to a seasonal variation in the column mean mole fraction X_{CH4} out of phase with tropospheric methane (Saad et al., 2014). Meridional transport in the stratosphere tends to be too fast in models, so that stratospheric methane concentrations at high latitudes are overestimated (Patra et al., 2011). Not correcting for this effect in inversions can lead to a 5% overestimate of methane emissions at northern mid-latitudes and a 40% overestimate in the Arctic (Ostler et al., 2015). Quantifying emissions from boreal wetlands is severely compromised.

A number of observational data sets are available to evaluate the stratospheric methane simulation in CTMs. These include balloons (Bergamaschi et al., 2013), TCCON stratospheric retrievals (Saad et al., 2014), and satellite observations by solar occultation and in the limb (deMaziere et al., 2008; von Clarmann et al., 2009; Noel et al., 2011; Minschwaner and Manney, 2014). Bergamaschi et al. (2013) presented a detailed evaluation of their CTM with balloon observations as prelude to inversion of SCIAMACHY data, and this led them to limit their inversion to the 50^oS-50^oN latitudinal range where model bias was small. Another approach is to apply a latitudinal bias correction for the difference between the CTM and the satellite data (Turner et al., 2015). Ostler et al. (2015) presented a method to correct for stratospheric methane bias in CTMs by using constraints on the age of air in the stratosphere from vertical profiles of sulfur hexafluoride (SF_6).

Error characterization. Estimation of prior and observational error covariances is crucial for inverse modeling. Observational error is the sum of instrument and CTM errors. We discussed in Sect. 2.2 the characterization of instrument error by validation with suborbital data. CTM error variance can be estimated by intercomparison of different CTMs (Patra et al., 2011) and added to the instrument error variance in quadrature. An alternative is to estimate the total observational error variance by the residual error method (Heald et al., 2004), which uses statistics of differences between the observations and the CTM simulation with prior emissions. In that method, systematic difference (bias) is assumed to be caused by error in emissions (to be corrected in the inversion), The remaining residual difference (averaging to zero) defines the total observational error, including contributions from instrument and CTM errors. This method has the merit of being consistent with the premise that the observational error is random. The CTM error variance can then be deduced by subtraction of the instrument error variance. Application to SCIAMACHY and GOSAT shows that the instrument error tends to be dominant (Wecht et al., 2014a; Turner et al., 2015). Error correlation populating the off-diagonal terms of the observational error covariance matrix is typically specified as an e-folding characteristic length scale (Heald et al., 2004).

Error in the prior bottom-up emission inventory can be estimated by propagation of errors in the variables used to construct the inventory (EPA, 2016), or by comparison of independently generated inventories such as the WETCHIMP intercomparison for wetlands (Melton et al., 2013) or regional anthropogenic inventories in the US (Maasakkers et al., 2016). Error PDFs are usually assumed to be normal or log-normal, but more skewed PDFs may better capture the occurrence of "super-emitters" (Zavala-Areiza et al., 2015). Errors may be scale-dependent, such that spatial aggregation of emission grid squares in the inversion decreases the error variance (Maasakkers et al., 2016). The prior error covariance matrix is usually taken to be diagonal, but some error correlation would in fact be expected for a given source sector. This is accounted for in the geostatistical inversion approach (Eq. (11)) by assuming coherence in source patterns.

Sources completely missing from the prior bottom-up inventory pose a particular difficulty for inverse modeling, because inverse methods applied to an underconstrained problem will tend to correct emissions where the prior estimate indicates them to be. Simply increasing the error on the prior estimate is not a satisfactory approach because the inverse solution may then misplace emissions. Before conducting the inversion it is important to compare the CTM simulation using prior emissions to the observations, and diagnose whether any elevated values in the observations that are absent in the simulation could represent missing sources.

3.3 Applications to SCIAMACHY and GOSAT data

Most inversions of SCIAMACHY and GOSAT satellite data for atmospheric methane have been done on the global scale, estimating emissions at the resolution of the CTM used as forward model (typically a few hundred km) by applying an adjoint method (Bergamaschi et al., 2009, 2013; Spahni et al., 2011; Monteil et al., 2013; Cressot et al., 2014; Houweling et al. 2014; Alexe et al., 2015). Fraser et al. (2013) estimated monthly methane fluxes over continental-scale source regions by using an analytical method with a Kalman filter. Wecht et al. (2014a) and Turner et al. (2015) used continental-scale inversions for North America to estimate emissions at up to 50 km resolution in source regions through optimal selection of the state vector, with Turner et al. (2015) applying an analytical inversion to characterize errors. Fraser et al. (2014) and Pandey et al. (2015) optimized both methane and CO_2 fluxes using X_{CH4}/X_{CO2} ratios observed from GOSAT, thus avoiding the need for independent specification of CO_2 concentrations in the CO_2 proxy method for methane retrieval. Cressot et al. (2014) and Alexe et al. (2015) compared results from inversions using different SCIAMACHY and GOSAT retrievals, and found overall consistency in different regions of the world; however, Cressot et al. (2014) pointed out large errors when using the degraded post-2005 SCIAMACHY data (see Sect. 2.2).

Inversions of methane fluxes using GOSAT data show consistency with observations from NOAA ESRL surface sites, both in joint inversions (Bergamaschi et al., 2009, 2013; Fraser et al., 2013; Alexe et al., 2015) and in independent evaluations (Turner et al., 2015). GOSAT observations are sparse, with observation points separated by about 260 km, but still provide considerably more information on methane emissions at the continental scale than the surface network observations (Fraser et al., 2013; Alexe et al., 2015). This is particularly true in the tropics, where methane emissions are large but surface observations are few (Bergamaschi et al., 2013; Cressot et al., 2014; Houweling et al., 2014).

Inversions of SCIAMACHY and GOSAT data have revealed important biases in bottom-up inventories of methane emissions. Monteil et al. (2013) and Spahni et al. (2011) find large errors in wetland emission models. Bergamaschi et al. (2013) find that 2003-2010 growth in Chinese emissions is less than estimated by EDGAR. Inversion results in the US show that EDGAR emissions in the South-Central US are too low while emissions along the East Coast are too high (Wecht et al., 2014a; Alexe et al., 2015; Turner et al., 2015).

Ultimately, the application of satellite data to improve understanding of methane emissions requires that the optimized estimates from the inversions be related to specific source sectors and processes in the bottom-up inventories. SCIAMACHY observations over wetlands have been used in this manner to improve bottom-up models of wetland emissions (Bloom et al., 2010, 2012; Spahni et al., 2011). Application of satellite observations to improve anthropogenic emission inventories has so far been stymied by poor representation of emission patterns in the inventories. For example, the EDGAR underestimate in the South-Central US cannot be confidently attributed to livestock or oil/gas sectors because EDGAR emission patterns for these sectors are incorrect (Maasakkers et al., 2016).

Satellite data sets for correlative variables could help relate methane observations to source sectors but this has received little attention so far. Bloom et al. (2012) combined methane data from SCIAMACHY with water height data from the GRACE satellite instrument to improve their bottom-up inventory of wetland methane emissions. Worden et al. (2012) combined measurements of methane and CO from TES to quantify methane emissions from Indonesian fires. TIR measurements of ammonia are available from the TES, IASI, and CrIS satellite instruments (Shephard et al., 2011; Van Damme et al., 2014; Shephard and Cady-Pereira, 2015) and provide a fingerprint of agricultural emissions (Zhu et al., 2013), but have yet to be exploited in combination with methane satellite data. Interpretation of the ammonia data is complicated by gas-aerosol partitioning with ammonium. In addition, ammonia is mainly emitted from manure and fertilizer, whereas methane is mostly from enteric fermentation and the sources may not be collocated. Ethane provides a marker for oil/gas emissions but is observed from space only by solar occultation with sensitivity limited to the upper troposphere (Abad et al., 2011). In addition, the ethane/methane emission ratio is highly variable. TROPOMI will provide data for both methane and CO from common SWIR retrievals. Beyond constraining the combustion source of methane, the CO observations could be valuable to decrease model transport errors in joint methane-CO inversions (Wang et al., 2009).

3.4 Potential of future satellite observations

Future satellite instruments listed in Table 1 will have higher pixel resolution, spatial density, and temporal frequency than SCIAMACHY or GOSAT. Several studies have examined how these attributes will improve the capability of methane flux inversions. Wecht et al. (2014b) conducted an inversion of methane emissions in California at $1/2^{o} \times 2/3^{o}$ resolution using boundary layer observations from the May-June 2010 CalNex aircraft campaign and concurrent observations from GOSAT. They then estimated the information that TROPOMI or the GEO-

CAPE geostationary mission would have provided over the 2-month period through analysis of the corresponding observational error correlation matrices. Inversion of the CalNex aircraft data provided 12 independent pieces of information (DOFS) on the spatial distribution of emissions in California as compared to 1.3 for GOSAT, 11 for TROPOMI, and 26 for GEO-CAPE. TROPOMI could thus constrain emissions with a skill comparable to a dedicated statewide aircraft campaign, and a geostationary mission with hourly observations would provide much more. The study likely underestimated the capability of TROPOMI and GEO-CAPE to resolve hotspots because of the coarse $1/2^{o} \times 2/3^{o}$ resolution of the forward model. We return to this point in Sect. 4.

Bousserez et al. (2016) explored the potential of geostationary observations to constrain methane emissions on the continental scale of North America over weekly and monthly time scales. Again they used a CTM with $1/2^{o} \times 2/3^{o}$ spatial resolution as forward model and averaged the 4×4 km^2 geostationary observation pixels over that coarser grid with corresponding error reduction. They considered three different configurations of geostationary instruments observing hourly in the SWIR, TIR, and SWIR+TIR (multispectral retrieval).They found that SWIR geostationary observations would effectively constrain methane emissions over the $1/2^{o} \times 2/3^{o}$ grid on a monthly time scale, while a combined SWIR+TIR instrument could deliver that information on a weekly time scale.

Bovensmann et al. (2010) examined the potential of CarbonSat to detect methane point sources by inversion of the Gaussian dispersion plume, and Rayner et al. (2014) did the same for geoCARB. We review their results in the next Section.

4. Observing requirements for regional and point sources

Here we present a simple analysis of the potential of future satellite instruments for observing regional and point sources from space. Observing requirements are somewhat different for climate policy and for point source monitoring purposes. From a climate policy standpoint, the goal is to quantify annual mean emissions with emphasis on the regional scale and source attribution. This plays to the strength of satellites, as repeated observations of the same scene measure the temporal average with improved precision, and also smooth out the temporal variability that can bias estimates from short-term field campaign data. From a point source monitoring standpoint, on the other hand, we may be most interested in detecting large leaks or venting from facilities emitting far more than would be expected on the basis of normal operations (the so-called "super-emitters"). Here the advantage of satellite data is spatial coverage, but a requirement is to have a localized and detectable signal on short time scales, with detection and localization being often more important than precise quantification.

For conceptual purposes we define detection/quantification as the ability to observe the methane enhancement ΔX [ppb] from a source relative to the surrounding background. Single-scene instrument precisions σ [ppb] are taken from Table 1, and we make the optimistic assumption that precision improves as the square root of the number of observations following the central limit theorem (Kulawik et al., 2016). We define detectability as a precision of $\Delta X/2$ and quantification as a precision of $\Delta X/5$. Only a fraction F of pixels is successfully retrieved because of clouds, unsuccessful spectral fits, or other factors. The time required for detection/quantification of the source is then

$$t = t_R \max\left[1, \frac{1}{FN}\max[1, \left(\frac{q\sigma}{\Delta X}\right)^2]\right] \quad (12)$$

where N is the number of observations of the source for a single satellite pass, t_R is the time interval between passes, and q takes on values of 2 for detection and 5 for quantification.

We first examine the capability of satellite instruments to quantify emissions from a large source region by taking as example the Barnett Shale in Northeast Texas, a 300×300 km^2 region with about 30,000 active wells as well as livestock operations and the Dallas/Fort Worth metropolitan area. An intensive field campaign was conducted in the region in September-October 2013 to characterize individual sources (Harriss et al., 2015). Synthesis of the data by Lyon et al. (2015) gives a total emission for the region of 72 tons h^{-1}. Take the Barnett Shale region as a square of side W = 300 km ventilated by a uniform wind of speed U. The mean enhancement ΔX relative to the upwind background is obtained by mass balance:

$$\Delta X = \frac{M_a}{M_{CH4}}\frac{Qg}{UWp} \quad (13)$$

where M_a = 0.029 kg mol^{-1} and M_{CH4} = 0.016 kg mol^{-1} are the molecular weights of dry air and methane, p is the dry atmospheric surface pressure, and g = 9.8 m s^{-2} is the acceleration of gravity. Taking U = 5 km h^{-1} and p = 1000 hPa, and with Q = 72 tons CH_4 h^{-1}, we obtain ΔX = 8.5 ppb or 0.47%.

Table 2 summarizes the capabilities of the SWIR instruments in Table 1 to quantify such a source. GOSAT views 2-3 pixels for a 300×300 km^2 region on a given orbit in its routine survey mode and has a return time of 3 days. The single-retrieval precision of GOSAT is 0.7% or 13 ppb. 17% of GOSAT land pixels are retrieved successfully on average in the Parker et al. (2011) CO_2 proxy retrieval (F = 0.17). Replacement into Eq. (12) implies that it takes about 1 year for GOSAT to effectively quantify emissions from the Barnett Shale. This explains why inverse analyses of GOSAT data retain substantial information from the prior as diagnosed by the averaging kernel matrix (Turner et al., 2015). A similar averaging time requirement applies to SCIAMACHY (2003-2005), which has denser observations but coarser precision and a smaller fraction of successful retrievals (F = 0.09). GOSAT-2 with an expected single-retrieval precision of 0.4% would reduce this time to about 4 months. TROPOMI will have full daily coverage of the Barnett Shale region with about 1,000 observing pixels, thus quantifying the regional emissions in a single day of observation.

Consider now the problem of detecting individual point sources through observations of the corresponding source pixels. We estimate for the different solar back-scatter instruments of Table 1 the detection threshold at the scale of a satellite pixel, and for a single observation pass, by assuming low emissions in neighboring pixels (to characterize a local background) and clear skies (for favorable retrieval conditions). The enhancement ΔX in the source pixel is given by equation (13) but with W now representing the pixel size and with N =1 and F = 1 in equation (12). By combining equations (12) and (13) we derive the minimum source Q_{min} for single-pass detection as

$$Q_{\min} = \frac{M_{CH4}}{M_a}\frac{UWpq\sigma}{g} \qquad (14)$$

Table 2 gives the detection thresholds for the different satellite instruments with $U = 5$ km h^{-1}. These values can be compared to detailed point source information available for the US. Figure 8 shows the high end of the distributions of annual emissions for (1) the gridded 0.1°×0.1° EPA inventory of Maasakkers et al. (2016), and (2) the 6887 individual point sources reporting methane emissions to the EPA Greenhouse Gas Reporting Program (GHGRP). Reporting to the GHGRP is required for all sources in excess of 25 Gg CO_2 equivalent a^{-1} (corresponding to 0.1 tons CH_4 h^{-1} for a pure methane source). The GHGRP data include combustion sources with very low methane emissions, hence Figure 8 only shows the top 15th percentile of point sources (accounting for 85% of total GHGRP methane emissions). The largest point sources in the GHGRP data with emissions in excess of 1 ton h^{-1} are underground coal mines and landfills; individual point sources from oil/gas systems (compressor stations, processing plants) are smaller. Emissions from natural gas production (including wells and gathering stations) are reported to the GHGRP as basin totals instead of as point sources and are thus not included in the point source distribution of Fig. 8 (but are included in the gridded emissions). Individual "super-emitters" in oil/gas fields can emit in excess of 1 ton h^{-1} but this is likely on an intermittent basis (Zavala-Areiza et al., 2015; Lyon et al., 2015).

Pixel resolution of the satellite instrument can be a limiting factor for detecting individual point sources because these are often clustered on a 1-10 km scale (as in an oil/gas field) and/or overlap with large area sources (gas distribution, livestock) (Lyon et al., 2015). For a satellite instrument with pixel resolution ~10 km, the frequency distribution of gridded 0.1°×0.1° (≈10×10 km^2) emissions in Fig. 8 is more relevant than that of GHGRP point sources.

Comparison of the detection thresholds in Table 2 to the emission distributions in Fig. 8 offers insight into the capabilities of the different instruments for resolving point sources. With a detection limit of 4 tons h^{-1} (for a wind of 5 km h^{-1}), TROPOMI can detect in a single pass the 20 highest 0.1° × 0.1° pixels in the gridded EPA inventory, contributing 5% of national emissions. It would not detect a typical transient "super-emitter" of 1.0 tons h^{-1} in an oil/gas field in a single overpass. Because of its full daily coverage, TROPOMI can be far more effective at detecting sustained point sources and quantifying their annual emissions. For 365 successive passes (once a day) and a successful retrieval rate of 17%, TROPOMI should be able to isolate individual pixel sources of 0.5 tons h^{-1}, representing the top 1% of 0.1° × 0.1° gridsquares in the EPA inventory and amounting to 30% of total US emissions. GOSAT-2 has a similar single-pass sensitivity to point sources as TROPOMI when observing in target mode but has much sparser coverage.

GHGSat and CarbonSat are designed for observation of point sources. If it meets its specifications of Table 1, GHGSat will have a single-pass detection threshold of 0.24 tons h^{-1} (for a wind of 5 km h^{-1}). This will detect 700 of the GHGRP point sources in Fig. 8, corresponding to 80% of the national total in the GHGRP point source inventory. A single GHGSat instrument will have a return time of 2 weeks, limiting its ability to detect transient "super-emitters", but long-term plans are for a fleet of instruments on microsatellites.

Bovensmann et al. (2010) give a CarbonSat detection threshold of 0.24 tons h^{-1} for $U = 5$ km h^{-1}, based on inversion of data from a transported Gaussian plume. We find a threshold of 0.8 tons h^{-1} for single-pixel detection. Mapping of the methane plume in downwind pixels offers additional opportunity for detecting/quantifying a point source as long as there is no overlap with other sources and some model of plume transport is applied. Bovensmann et al. (2010) did not include transport error in their analysis which may lead to overoptimistic results. With 2×2 km^2 pixel resolution, CarbonSat would be limited in its ability to resolve the structure of individual methane plumes, as airborne mapping shows plumes to be smaller in scale even for large point sources (Krings et al., 2013; Thorpe et al., 2016; Frankenberg et al., 2016). The 0.05×0.05 km^2 resolution of GHGSat, with imaging over a 12 × 12 km^2grid, has better potential for resolving the plume structure. A complication in remote sensing of plumes with sub-km pixels is that one may not assume that the incident and reflected solar rays (Fig. 2) sample the same boundary layer methane column. The air mass factor calculation must trace the propagation of the incident and reflected solar rays through the plume, taking into account the solar azimuth and zenith angles as well as the altitude of the plume.

Several approaches have been used to exploit downwind plume information for inferring point source emissions, including (1) inverse modeling with source strength and dispersion parameters as state variables (Krings et al., 2011, 2013), (2) integrating the flux over the plume cross-section normal to wind direction (Conley et al., 2016), and (3) summing the above-background mass in all plume pixels and relating this integrated mass enhancement to emission by using a relationship from known sources or a plume dispersion model (Frankenberg et al., 2016). Choice of the best approach may depend on the level of meteorological information available and the ability of the instrument to map the observed plume structure, which in turn depends on the pixel size, the measurement noise, the ability to define the local background, and the complexity of the flow including the effect of wind shear (Rayner et al., 2014).

Geostationary observations can in principle achieve high precision together with fine pixel resolution because the viewing geometry allows much longer observation times. But there is competing demand for spatial coverage. Currently proposed geostationary missions (Table 1) expect to achieve 0.2-1% precision for pixels 2-5 km in size, limited in part by their stated mission objectives to observe continental-scale domains several times a day. With this implementation and the above assumptions, a regional source such as the Barnett Shale is strongly constrained on a single-pass basis but the capability to detect transient point sources is limited (Table 2). Point sources could be detected more effectively from geostationary orbit by adopting longer viewing times per pixel and/or using finer pixels. This could be achieved by limiting the domain of observation or by using “special observations” where the instrument is maneuvered to stare at specific points of interest. For example, detection of an anomaly in emissions, either from the satellite or from suborbital observations, could motivate targeted observation by the satellite to localize and quantify the anomaly. A schedule of alternate days for continental-scale mapping and for special observations could be effective to quantify emissions at the national and regional scales while also providing fast detection and quantification of point sources.

Airborne remote sensing offers another way to observe methane emissions from point sources, using the same techniques as satellite remote sensing but with much higher spatial resolution. MAMAP (Krings et al., 2011) retrieves methane in the SWIR at 1.6μm, similar to SCIAMACHY, but currently lacks imaging capabilities. Imaging spectrometers initially designed for surface remote sensing have been shown to detect methane plumes with horizontal resolution as fine as 1 m either in the SWIR using the strong 2.3 μm band (Roberts et al., 2010; Thorpe et al,, 2016)) or in the TIR (Tratt et al, 2014; Hulley et al, 2016). These imaging spectrometers such as AVIRIS-NG (SWIR) and MAKO or HyTES (TIR) have much coarser spectral resolution than MAMAP or current satellite instruments (e.g., 5 nm for AVIRIS-NG).

However, at this fine spatial resolution, concentration enhancements over point sources are much higher and can be discerned down to a detection threshold of only 2 kg h^{-1} (Thorpe et al., 2016). A major advantage is that the fine structure of the plume shape can be observed, allowing for localized source attribution (Thompson et al., 2015; Thorpe et al, 2016).

5. Conclusions and recommendations

We have reviewed the capabilities for observing atmospheric methane from space and their utility for improving knowledge of methane emissions through inverse analyses. Observations in the shortwave infrared (SWIR) are of most interest for quantifying emissions because they are sensitive to the full atmospheric column down to the surface. Retrievals combining the SWIR and the thermal infrared (TIR) would isolate the lower tropospheric contribution to methane and thus reduce uncertainties in accounting for the free tropospheric background and the stratosphere.

Current SWIR observations from the GOSAT satellite are of high quality but sparse. Through inverse analyses and annual averaging they can quantify emissions in source regions on a 100-1000 km scale. The TROPOMI instrument to be launched in 2017 will be able to map emissions daily on that scale and will also have the capability to detect and quantify large point sources. As such it will significantly enhance the value of satellite measurements to serve the needs of climate policy. The GHGSat instrument launched in 2016 with 50 × 50 m^2 pixel resolution over 12 ×12 km^2 viewing domains will effectively detect methane point sources if it meets its specification of 1-5% precision. Arctic sources of methane are difficult to observe from space because of limited solar radiation and because of uncertainty in accounting for stratospheric methane. Future lidar observations from MERLIN offer a unique resource to observe the Arctic under dark conditions, and the influence of the stratosphere could be removed by using combined SWIR and TIR retrievals or by using limb and solar occultation measurements.

The ultimate goal of top-down inverse analyses of atmospheric observations is to guide the improvement of bottom-up emission inventories relating emissions to the underlying processes There is the opportunity for considerable synergy between top-down and bottom-up approaches by using high-quality bottom-up inventories as prior estimates in inversions, and then using inversion results to improve the inventories. Exploiting this synergy requires the construction of finely gridded, sector-resolved bottom-up inventories including error estimates.

Geostationary observations (still at the proposal stage) hold considerable potential for monitoring methane emissions from space. The geostationary orbit allows sustained staring at individual pixels, providing a unique opportunity to infer emissions with both high spatial and temporal resolution on national scales. This also enables the characterization of diurnally varying sources such as from wetlands (Makkela et al., 1995) and manure (Wood et al., 2013), where LEO sun-synchronous observations at a single time of day might provide a biased estimate. Current geostationary mission proposals emphasize hourly mapping of emissions at the continental scale. This limits their pixel resolution and their precision. It is not clear that high-frequency continental-scale mapping from geostationary orbit is of much value if sufficient information is already available from a LEO instrument such as TROPOMI. It may be more effective for a geostationary mission to focus on selective observation of point sources and source regions, enabling finer pixel resolution and longer viewing times to resolve emissions at local scale including transient sources.

More work needs to be done in exploiting correlative observations to increase the value of methane satellite data, but the task is difficult because of the uniqueness of methane sources. Observations of ammonia from space are becoming mature and provide a marker of agricultural operations though the sources of ammonia (fertilizer, manure) only partly overlap with the sources of methane (enteric fermentation, manure). Joint observations of methane and CO as from TROPOMI may help to reduce model transport error in inversions through methane-CO error correlations. Satellite mapping of surface properties can provide important correlative information, as already demonstrated for wetlands. Satellite data for soil moisture, gas flaring, and imagery of point sources could be integrated with available methane data to more effectively constrain methane emissions.

Suborbital observations of methane from aircraft and from the ground are essential partners to satellite observation. Suborbital observations have unique capability for correlative measurements such as methane isotopes and ethane that can provide additional constraints in inversions. They can confirm methane anomalies detected from space, and pinpoint sources with far greater accuracy (down to the device scale) than is achievable from space. Suborbital platforms are also essential for continual validation of the satellite data. The prospect of improving satellite observations in the near future calls for the construction of a comprehensive atmospheric methane observing system to monitor emissions from global to local scales through coordination with improved suborbital observations, bottom-up inventories, and atmospheric transport models.

Acknowledgments. This work was funded by the NASA Carbon Monitoring System, by the NASA GEO-CAPE Atmospheric Sciences Working Group, by the ExxonMobil Upstream Research Company, and by the US DOE Advanced Research Projects Agency – Energy. KV acknowledges funding from the Smithsonian Astrophysical Observatory. We thank Helen Worden for pointing out an error in the original submitted paper.

References

Abad, G.G., et al., Ethane, ethyne and carbon monoxide concentrations in the upper troposphere and lower stratosphere from ACE and GEOS-Chem: a comparison study, Atmos. Chem. Phys., 11, 9927–9941, 2011.

Alexe, M., P. Bergamaschi, A. Segers, R. Detmers, A. Butz, O. Hasekamp, S. Guerlet, R. Parker, H. Boesch, C. Frankenberg, R. A. Scheepmaker, E. Dlugokencky, C. Sweeney, S. C. Wofsy, and E. A. Kort, Inverse modelling of CH_4 emissions for 2010–2011 using different satellite retrieval products from GOSAT and SCIAMACHY, Atmos. Chem. Phys., 15, 113–133, 2015.

Anderson, G., S. Clough, F. Kneizys, J. Chetwynd, and E. Shettle, AFGL atmospheric constituent profiles (0–120 km), Tech. Rep. AFGL-TR-86-0110, Air Force Geophys. Lab., Hanscom Air Force Base, Bedford, Mass., 1986.

Andrews, A. E., Kofler, J. D., Trudeau, M. E.,Williams, J. C., Neff, D. H., Masarie, K. A., Chao, D. Y., Kitzis, D. R., Novelli, P. C., Zhao, C. L., Dlugokencky, E. J., Lang, P. M., Crotwell, M.J., Fischer, M. L., Parker, M. J., Lee, J. T., Baumann, D. D., Desai, A. R., Stanier, C. O., De Wekker, S. F. J., Wolfe, D. E., Munger, J. W., and Tans, P. P.: CO2, CO, and CH4 measurements from tall towers in the NOAA Earth System Research Laboratory's Global Greenhouse Gas Reference Network: instrumentation, uncertainty analysis, and recommendations for future high-accuracy greenhouse gas monitoring efforts, Atmos. Meas. Tech., 7, 647–687, 2014.

Barnet, C., et al., CrIS Trace Gas Data Users Workshop, 18 Sept 2014.

Benmergui, J., et al., Integrating diverse observations of North American CH_4 into flux inversions in CarbonTrackerLagrange-CH_4, presented at the Fall 2015 meeting of the American Geophysical Union, 2015.

Bergamaschi, P., Krol, M., Dentener, F., Vermeulen, A., Meinhardt, F., Graul, R., Ramonet, M., Peters, W. and Dlugokencky, E.: Inverse modelling of national and European CH4 emissions using the atmospheric zoom model TM5, Atmos. Chem. Phys., 5, 2431–2460, 2005.

Bergamaschi, P., C. Frankenberg, J. F. Meirink, M. Krol, M. G. Villani, S. Houweling, F. Dentener, E. J. Dlugokencky, J. B. Miller, L. V. Gatti, A. Engel, and I. Levin, Inverse modeling of global and regional CH_4 emissions using SCIAMACHY satellite retrievals, J. Geophys. Res., 114, doi:10.1029/2009JD012287, 2009.

Bergamaschi, P., S. Houweling, A. Segers, M. Krol, C. Frankenberg, R. A. Scheepmaker, E. Dlugokencky, S. C. Wofsy, E. A. Kort, C. Sweeney, T. Schuck, C. Brenninkmeijer, H. Chen, V. Beck, and C. Gerbig, Atmospheric CH4 in the first decade of the 21st century: Inverse modeling analysis using SCIAMACHY satellite retrievals and NOAA surface measurements, J. Geophys. Res. Atmos., 118, 7350–7369, 2013.

Bloom, A.A., P.I. Palmer, A. Fraser, and D.S. Reay, Seasonal variability of tropical wetland CH4 emissions: the role of the methanogen-available carbon pool, Biogeosciences, 9, 2821–2830, 2012.

Bousquet, P., et al., Contribution of anthropogenic and natural sources to atmospheric methane variability, Nature, 443, 439-443, 2006.

Bousquet, P., B. Ringeval, I. Pison, E. J. Dlugokencky, E.-G. Brunke, C. Carouge, F. Chevallier, A. Fortems-Cheiney, C. Frankenberg, D. A. Hauglustaine, P. B. Krummel, R. L. Langenfelds, M. Ramonet, M. Schmidt, L. P. Steele, S. Szopa, C. Yver, N. Viovy and P. Ciais, Source attribution of the changes in atmospheric methane for 2006-2008, Atmos. Chem. Phys., 11, 3689–3700, 2011.

Bousserez, N., et al., Improved analysis-error covariance matrix for high-dimensional variational inversions: application to source estimation using a 3D atmospheric transport model, QJRMS, DOI:10.1002/qj.2495, 2015.

Bousserez, N., D.K. Henze, B. Rooney, A. Perkins, K.J Wecht, A.J. Turner, V. Natraj, and J.R. Worden, Constraints on methane emissions in North America from future geostationary remote sensing measurements, Atmos. Chem. Phys. Discuss., 15, 19017–19044, 2016.

Bovensmann, H., M. Buchwitz, J.P. Burrows, M. Reuter, T. Krings, K. Gerilowski, O. Schneising, J. Heymann, A. Tretner, and J. Erzinger, A remote sensing technique for global monitoring of power plant CO_2 emissions from space and related applications, Atmos. Meas. Tech., 3, 781–811, 2010.

Brakeboer, B.N.A., Development of the structural and thermal control subsystems for an Earth observation microsatellite and its payload, M.S. Thesis, University of Toronto, 2015.

Brandt, A.R., et al., Methane leaks from North American gas systems, Science, 343, 733-735, 2014.

Brasseur, G.P., and D.J. Jacob, Modeling of Atmospheric Chemistry, Cambridge University Press, New York, 2016.

Bruhwiler, L., E. Dlugokencky, K. Masarie, M. Ishizawa, A. Andrews, J. Miller, C. Sweeney, P. Tans, and D. Worthy, CarbonTracker-CH4: an assimilation system for estimating emissions of atmospheric methane, Atmos. Chem. Phys., 14, 8269–8293, 2014.

Buchwitz, M., M. Reuter, H. Bovensmann, D. Pillai, J. Heymann, O. Schneising, V. Rozanov, T. Krings, J. P. Burrows, H. Boesch, C. Gerbig, Y. Meijer, and A. Löscher, Carbon Monitoring Satellite (CarbonSat): assessment of atmospheric CO_2 and 4 retrieval errors by error parameterization, Atmos. Meas. Tech., 6, 3477–3500, 2013.

Buchwitz, M., et al., The Greenhouse Gas Climate Change Initiative (GHG-CCI): Comparison and quality assessment of near-surface-sensitive satellite-derived CO_2 and CH_4 global data sets, Remote Sensing Environ., 162, 344-362, 2015.

Buchwitz, M., O. Schneising, M. Reuter, J. Heymann, S. Krautwurst, H. Bovensmann, J.P. Burrows, H. Boesch, R.J. Parker, R.G. Detmers, O.P. Hasekamp, I. Aben, A. Butz, and C. Frankenberg, Satellite-derived methane hotspot emission estimates using a fast data-driven method, Atmos. Chem. Phys. Discuss., doi:10.5194/acp-2016-755, 2016.

Bui-Thanh, T., C. Burstedde, O. Ghattas, J. Martin, G. Stadler, and L.C. Wilcox (2012), Extreme-scale UQ for Bayesian inverse problems governed by PDEs, in IEEE International Conference for High Performance Computing, Networking, Storage and Analysis, Salt Lake City, Utah, Nov 2012.

Butz, A., O.P. Hasekamp, C. Frankenberg, and I. Aben, Retrievals of atmospheric CO2 from simulated space-borne measurements of backscattered near-infrared sunlight: accounting for aerosol effects, Appl. Opt., 48, 3322-3336, 2010.

Butz, A., et al., Toward accurate CO_2 and CH_4 observations from GOSAT, Geophys. Res. Lett., 38, L14812, 2011.

Butz, A., Galli, A., Hasekamp, O., Landgraf, J., Tol, P., and Aben, I.: TROPOMI aboard Precursor Sentinel-5 Precursor: Prospective performance of CH4 retrievals for aerosol and cirrus loaded atmospheres, Remote Sens. Environ., 120, 267–276, 2012.

Butz, A., J. Orphal, R. Checa-Garcia, F. Friedl-Vallon, T. von Clarmann, H. Bovensmann, O. Hasekamp, J. Landgraf, T. Knigge, D. Weise, O. Sqalli-Houssini, and D. Kemper, Geostationary Emission Explorer for Europe (G3E): mission concept and initial performance assessment, Atmos. Meas. Tech., 8, 4719–4734, 2015.

Caulton, D.R., et al., Toward a better understanding and quantification of methane emissions from shale gas development, PNAS, 111, doi: 10.1073/pnas.1316546111, 2014.

Clerbaux, C., J. Hadji-Lazaro, S. Turquety, G. Megie, and P.-F. Coheur, Trace gas measurements from infrared satellite for chemistry and climate applications, Atmos. Chem. Phys., 3, 1495–1508, 2003.

Conley, S., G. Franco, I. Faloona, D.R. Blake, J. Peischl ,and T.B. Ryerson, Methane emissions from the 2015 Aliso Canyon blowout in Los Angeles, CA, Science, 351, 1317-1321, 2016.

Cressot, C., Chevallier, F., Bousquet, P., Crevoisier, C., Dlugokencky, E. J., Fortems-Cheiney, A., Frankenberg, C., Parker, R., Pison, I., Scheepmaker, R. A., Montzka, S. A., Krummel, P. B., Steele, L. P., and Langenfelds, R. L.: On the consistency between global and regional methane emissions inferred from SCIAMACHY, TANSO-FTS, IASI and surface measurements, Atmos. Chem. Phys., 14, 577-592, doi:10.5194/acp-14-577-2014, 2014.

Crevoisier, C., et al., The 2007–2011 evolution of tropical methane in the mid-troposphere as seen from space by MetOp-A/IASI, Atmos. Chem. Phys., 13, 4279–4289, 2013.

De Maziere, M., et al., Validation of ACE-FTS v2.2 methane profiles from the upper troposphere to the lower mesosphere, Atmos. Chem. Phys., 8, 2421–2435, 2008

Dils, B., et al., The Greenhouse Gas Climate Change Initiative (GHG-CCI): comparative validation of GHG-CCI SCIAMACHY/ENVISAT and TANSO-FTS/GOSAT CO_2 and CH_4 retrieval algorithm products with measurements from the TCCON, Atmos. Meas. Tech., 7, 1723–1744, 2014.

Dlugokencky, E. J., L. Bruhwiler, J. W. C. White, L. K. Emmons, P. C. Novelli, S. A. Montzka, K. A. Massie, P. M. Lang, A. M. Crotwell, J. B. Miller and L. V. Gatti, Observational constraints on recent increases in the atmospheric CH_4 burden, Geophys. Res. Lett., 36, L18803, 2009.

Dlugokencky, E. J., E. G. Nisbet, R. Fisher and D. Lowry, Global atmospheric methane: budget, changes and dangers, Phil. Trans. Roy. Soc. A 369, no. 1943, 2058-2072, 2011.

Dlugokencky, E., Lang, P. M., Crotwell, A. M., Masarie, K. A., and Crotwell, M. J.: Atmospheric methane dry-air mole fractions from the NOAA ESRL carbon cycle cooperative global air sampling network: 1988–2012, version: 2013-06-18, ftp://ftp.cmdl.noaa.gov/ccg/ch4/flask/surface, 2013.

European Commission, Joint Research Centre, and Netherlands Environmental Assessment Agency, Emission database for global atmospheric research (EDGAR), http://edgar.jrc.ec.europa.eu, Release version 4.2, 2011.

Fishman, J., L. et al., The United States' next generation of atmospheric composition and coastal ecosystem measurements: NASA's Geostationary Coastal and Air Pollution Events (GEO-CAPE) Mission, BAMS, doi: 10.1175/BAMS-D-11-00201.1, 2012.

Frankenberg, C., U. Platt, and T. Wagner. Iterative maximum a posteriori (IMAP)-DOAS for retrieval of strongly absorbing trace gases: Model studies for CH4 and CO2 retrieval from near infrared spectra of SCIAMACHY onboard ENVISAT, Atmos. Chem. Phys., 5, 9–22, 2005

Frankenberg, C., Meirink, J. F., Bergamaschi, P., Goede, A. P. H., Heimann, M., Körner, S., Platt, U., van Weele, M., and Wagner, T.: Satellite chartography of atmospheric methane from SCIAMACHY on board ENVISAT: Analysis of the years 2003 and 2004, J. Geophys. Res., 111, D07303, 2006.

Frankenberg, C., I. Aben, P. Bergamaschi, E. J. Dlugokencky, R. van Hees, S. Houweling, P. van der Meer, R. Snel, P. Tol, Global column averaged methane mixing ratios from 2003 to 2009 as derived from SCIAMACHY: Trends and variability, J. Geophys. Res., 116, D04302, 2011.

Frankenberg, C., A.K. Thorpe, D.R. Thompson, G. Hulley, E.A. Kort, N. Vance, J. Borchardt, T. Krings, K. Gerilowski, C. Sweeney, S. Conley, B.D.. Bue, A.D. Aubrey, S. Hook, and R.O. Green, Airborne methane remote measurements reveal heavy-tail flux distribution in the Four Corners region, PNAS, 113, 9734-9739, 2016.

Fraser, A., et al., Estimating regional methane surface fluxes: the relative importance of surface and GOSAT mole fraction measurements, Atmos. Chem. Phys., 13, 5697-5713, 2013.

Fraser, A., et al. Estimating regional fluxes of CO2 and CH4 using space-borne observations of XCH4 :XCO2, Atmos. Chem. Phys., 14, 12883–12895, 2014.

Ganesan, A.L., et al., Characterization of uncertainties in atmospheric trace gas inversions using hierarchical Bayesian methods, Atmos. Chem. Phys., 14, 3855–3864, 2014.

Ganesan, A.L., A. J. Manning, A. Grant, D. Young, D. E. Oram, W. T. Sturges, J. B. Moncrieff, and S. O'Doherty, Quantifying methane and nitrous oxide emissions from the UK and Ireland using a national-scale monitoring network Atmos. Chem. Phys., 15, 6393–6406, 2015

Gloudemans, A.M.S., H. Schrijver, O. P. Hasekamp, and I. Aben, Error analysis for CO and CH4 total column retrievals from SCIAMACHY 2.3μm spectra, Atmos. Chem. Phys., 8, 3999–4017, 2008.

Glumb, R., G. Davis, and C. Lietzke, The TANSO-FTS-2 instrument for the GOSAT-2 Greenhouse Gas Monitoring Mission, IEEE International Symposium on Geoscience and Remote Sensing IGARSS, 1238-1240, 2014.

Harriss, R.C., et al., Using Multi-Scale Measurements to Improve Methane Emission Estimates from Oil and Gas Operations in the Barnett Shale Region, Texas, Environ. Sci. Technol. 49, 7524−7526, 2015.

Hartmann, D.L., et al., Observations: atmosphere and surface. In: Climate Change 2013: The Physical Science Basis. Contribution of Working Group I to the Fifth Assessment Report of the Intergovernmental Panel on Climate Change [Stocker, T.F., D. Qin, G.-K. Plattner, M. Tignor, S.K. Allen, J. Boschung, A. Nauels, Y. Xia, V. Bex and P.M. Midgley (eds.)]. Cambridge University Press, Cambridge, United Kingdom and New York, NY, USA, 2013.

Heald, C., Jacob, D., Jones, D., Palmer, P., Logan, J., Streets, D., Sachse, G., Gille, J., Hoffman, R., and Nehrkorn, T.: Comparative inverse analysis of satellite (MOPITT) and aircraft (TRACE-P) observations to estimate Asian sources of carbon monoxide, J. Geophys. Res., 109, D23306, 2004.

Henne, S., et al. (2016), Validation of the Swiss methane emission inventory by atmospheric observations and inverse modelling, Atmos. Chem. Phys., 16, 3683–3710.

Henze, D. K., A. Hakami, and J. H. Seinfeld, Development of the adjoint of GEOS-Chem, Atmos. Chem. Phys., 7, 2413–2433, 2007.

Herbin, H., L. C.-Labonnote, and P. Dubuisson, Multispectral information from TANSO-FTS instrument – Part 1:Application to greenhouse gases (CO2 and CH4) in clear sky conditions, Atmos. Meas. Tech., 6, 3301–3311, 2013.

Hiller, R.V., et al. (2016), Anthropogenic and natural methane fluxes in Switzerland synthesized within a spatially explicit inventory, Biogeosciences, 11, 1941–1960.

Houweling, S., Kaminski, T., Dentener, F., Lelieveld, J., and Heimann, M.: Inverse modeling of methane sources and sinks using the adjoint of a global transport model, J. Geophys. Res., 104, 26137–26160, 1999.

Houweling, S., M. Krol, P. Bergamaschi, C. Frankenberg, E. J. Dlugokencky, I. Morino, J. Notholt, V. Sherlock, D. Wunch, V. Beck, C. Gerbig, H. Chen, E. A. Kort, T. Röckmann, and I. Aben, A multi-year methane inversion using SCIAMACHY, accounting for systematic errors using TCCON measurements, Atmos. Chem. Phys. 14, 3991-4012, 2014.

Hulley, G. C., Duren, R. M., Hopkins, F. M., Hook, S. J., Vance, N., Guillevic, P., et al. (2016). High spatial resolution imaging of methane and other trace gases with the airborne Hyperspectral Thermal Emission Spectrometer (HyTES). Atmospheric Measurement Techniques Discussions, 1-32, 2016.

IPCC, 2006 IPCC Guidelines for National Greenhouse Gas Inventories, Prepared by the National Greenhouse Gas Inventories Programme, Eggleston H.S., Buendia L., Miwa K., Ngara T. and Tanabe K. (eds). IGES, Japan, 2006.

Kaminski, T., Rayner, P. J., Heimann, M., and Enting, I. G.: On aggregation errors in atmospheric transport inversions, J. Geophys. Res., 106, 4703, 2001.

Karion, A., C. Sweeney, G. Pétron, G. Frost, R. M. Hardesty, J. Kofler, B. R. Miller, T. Newberger, S. Wolter, R. Banta, A. Brewer, E. Dlugokencky, P. Lang, S. A. Montzka, R. Schnell, P. Tans, M. Trainer, R. Zamora, and S. Conley, Methane emissions estimate from airborne measurements over a western United States natural gas field, Geophys. Res. Lett., 40, 4393–4397, doi:10.1002/grl.50811, 2013.

Karion, A., et al., Aircraft-Based Estimate of Total Methane Emissions from the Barnett Shale Region, Environ. Sci. Technol., 49, 8,124-8,131, 2015.

Kiemle, C., M. Quatrevalet, G. Ehret, A. Amediek, A. Fix, and M.Wirth, Sensitivity studies for a space-based methane lidar mission, Atmos. Meas. Tech., 4, 2195–2211, 2011.

Kiemle, C., S. R. Kawa, M. Quatrevalet, and E. V. Browell, Performance simulations for a spaceborne methane lidar mission, J. Geophys. Res. Atmos., 119, 4365–4379, 2014.

Kirschke, S., P. Bousquet, P. Ciais, M. Saunois, J. G. Canadell, E. J. Dlugokencky, P. Bergamaschi, D. Bergmann, D. R. Blake, L. Bruhwiler, P. Cameron-Smith, S. Castaldi, F. Chevallier, L. Feng, A. Fraser, M. Heimann, E. L. Hodson, S. Houweling, B. Josse, P. J. Fraser, P. B. Krummel, J.-F. Lamarque, R. L. Langenfelds, C. Le Quere, V. Naik, S. O'Doherty, P. I. Palmer, I. Pison, D. Plummer, B. Poulter, R. G. Prinn, M. Rigby, B. Ringeval, M. Santini, M. Schmidt, D. T. Shindell, I. J. Simpson, R. Spahni, L. P. Steele, S. A. Strode, K. Sudo, S. Szopa, G. R. van der Werf, A. Voulgarakis, M. van Weele, R. F. Weiss, J. E. Williams, and G. Zeng, Three decades of global methane sources and sinks, Nature Geosci, 6(10), 813-823,10.1038/ngeo1955, 2013.

Kleipool, Q.L., R.T. Jongma, A.M.S. Gloudemans, H. Schrijver, G.F. Lichtenberg, R.M. van Hees, A.N. Maurellis, R.W.M. Hoogeveen, In-flight proton-induced radiation damage to SCIAMACHY’s extended-wavelength InGaAs near-infrared detectors, Infrared Physics & Technology, 50, 30–37, 2007.

Kort, E. A., J. Eluszkiewicz, B. B. Stephens, J. B. Miller, C. Gerbig, T. Nehrkorn, B. C. Daube, J. O. Kaplan, S. Houweling, and S. C. Wofsy, Emissions of CH_4 and N_2O over the United States and Canada based on a receptor-oriented modeling framework and COBRA- NA atmospheric observations, Geophys. Res. Lett., 35, L18808, doi:10.1029/2008GL034031, 2008.

Kort, E. A., C. Frankenberg, K. R. Costigan, R. Lindenmaier, M. K. Dubey, and D. Wunch, Four corners: The largest US methane anomaly viewed from space, Geophys. Res. Lett., 41, 6898–6903, 2014.

Krings, T., K. Gerilowski, M. Buchwitz, M. Reuter, A. Tretner, J. Erzinger, D. Heinze, U. Pfluger, J.P. Burrows, and H. Bovensmann, MAMAP – a new spectrometer system for column-averaged methane and carbon dioxide observations from aircraft: retrieval algorithm and first inversions for point source emission rates, Atmos. Meas. Tech., 4, 1735–1758, 2011.

Krings, T., K. Gerilowski, M. Buchwitz, J. Hartmann, T, Sachs, J. Erzinger, J.P. Burrows, and H. Bovensmann, Quantification of methane emission rates from coal mine ventilation shafts using airborne remote sensing data, Atmos. Meas. Tech., 6, 151–166, 2013.

Kulawik, S., et al., Consistent evaluation of ACOS-GOSAT, BESD-SCIAMACHY, CarbonTracker, and MACC through comparisons to TCCON, Atmos. Meas. Tech., 9, 683–709, 2016.

Kuze, A., H. Suto, M. Nakajima, and T. Hamazaki, Thermal and near infrared sensor for carbon observation Fourier-transform spectrometer on the Greenhouse Gases Observing Satellite for greenhouse gases monitoring, Appl. Opt. , 48, 6,716-6,733, 2009.

Kuze, A., et al., Update on GOSAT TANSO-FTS performance, operations, and data products after more than six years in space, Atmos. Meas. Tech. Discuss, doi:10.5194/amt-2015-333, 2016

Lyon, D. R., Zavala-Araiza, D., Alvarez, R. A., Harriss, R., Palacios, V., Lan, X., Talbot, R., Lavoie, T., Shepson, P., Yacovitch, T. I., et al.. Constructing a spatially resolved methane emission inventory for the Barnett Shale region. Environ. Sci. Technol.,8147–8157, 2015.

Maasakkers, J.D., et al., A gridded national inventory of US methane emissions, Environ. Sci. Technol., in press, 2016.

Marais, E. A., D. J. Jacob , K. Wecht, C. Lerot, L. Zhang, K. Yu, T. P. Kurosu, K. Chance, and B. Sauvage,Anthropogenic emissions in Nigeria and implications for ozone air quality: a view from space, Atmos. Environ., 99, 32-40, 2014.

Marchese, A. J., Vaughn, T. L., Zimmerle, D. J., Martinez, D. M., Williams, L. L., Robinson, A. L., Mitchell, A. L., Subramanian, R., Tkacik, D. S., Roscioli, J. R., et al. (2015). Methane emissions from United States natural gas gathering and processing, Environ. Sci. Technol., 49, 10,718-10,727, 2015.

Melton, J. R., R. Wania, E. L. Hodson, B. Poulter, B. Ringeval, R. Spahni, T. Bohn, C. A. Avis, D. J. Beerling, G. Chen, A. V. Eliseev, S. N. Denisov, P. O. Hopcroft, D. P. Lettenmaier, W. J. Riley, J. S. Singarayer, Z. M. Subin, H. Tian, S. Zu¨rcher, V. Brovkin, P. M. vanBodegom, T. Kleinen, Z. C. Yu, and J. O. Kaplan, Present state of global wetland extent and wetland methane modelling: conclusions from a model inter-comparison project (WETCHIMP), Biogeosciences, 10 (2), 753–788, 2013.

Mikkela, C., et al. Diurnal variation in methane emission in relation to the water table, soil temperature, climate and vegetation cover in a Swedish acid mire, Biogeochemistry 28, 93-114, 1995.

Miller, S.M., S. C. Wofsy, A. M. Michalak, E. A. Kort, A. E. Andrews, S. C. Biraud, E. J. Dlugokencky, J. Eluskiewicz, M. L. Fisher, G. Janssens-Maenhout, B. R. Miller, J. B. Miller, S. A. Montzka, T. Nehrkorn, and C. Sweeney, Anthropogenic emissions of methane in the US, PNAS, doi:10.1073/pnas.1314392110, 2013.

Miller, S.M., A.M. Michalak, and P. J. Levi, Atmospheric inverse modeling with known physical bounds: an example from trace gas emissions, Geosci. Model Dev., 7, 303–315, 2014.

Minschwaner, K., and G.L. Manney, Derived methane in the stratosphere and lower mesosphere from Aura Microwave Limb Sounder measurements of nitrous oxide, water vapor, and carbon monoxide, J Atmos Chem., 71:253–267, 2014.

Mitchell, A.L., et al.. Measurements of Methane Emissions from Natural Gas Gathering Facilities and Processing Plants: Measurement Results, Environ. Sci. Technol., 49, 3,219-3,227, 2015.

Monteil, G., S. Houweling, A. Butz, S. Guerlet, D. Schepers, O. Hasekamp, C. Frankenberg, R. Scheepmaker, I. Aben, and T. Röckmann, Comparison of CH4 inversions based on 15 months of GOSAT and SCIAMACHY observations, J. Geophys. Res. Atmos., 118, doi:10.1002/2013JD019760, 2013.

Myhre, G., et al., Anthropogenic and Natural Radiative Forcing. In: Climate Change 2013: The Physical Science Basis. Contribution of Working Group I to the Fifth Assessment Report of the Intergovernmental Panel on

Climate Change [Stocker, T.F., D. Qin, G.-K. Plattner, M. Tignor, S.K. Allen, J. Boschung, A. Nauels, Y. Xia, V. Bex and P.M. Midgley (eds.)]. Cambridge University Press, Cambridge, United Kingdom and New York, NY, USA, 2013.

Ostler, A., et al., The imprint of stratospheric transport on column-averaged methane, Atmos. Chem. Phys. Discuss., 15, 20395–20447, 2015

Pandey, S., S. Houweling, M. Krol, I. Aben, and T. Röckmann, On the use of satellite-derived CH4 :CO2 columns in a joint inversion of CH4 and CO2 fluxes, Atmos. Chem. Phys., 15, 8615–8629, 2015

Parker, R., H. Boesch, A. Cougan, A. Fraser, L. Feng, P I. Palmer, J. Messerschmidt, N. Deutscher, D. W. T. Griffith, J. Notholt, P. O. Wennnberg and D. Wunch, Methane observations from the Greenhouse Gases Observing SATellite: Comparison to ground-based TCCON data and model calculations, Geophys. Res. Lett., 38, L15807, 2011.

Parker, R.J., et al., Assessing 5 years of GOSAT Proxy XCH4 data and associated uncertainties, Atmos. Meas. Tech., 8, 4785–4801, 2015.

Patra, P.K., et al., TransCom model simulations of CH4 and related species: linking transport, surface flux and chemical loss with CH4 variability in the troposphere and lower stratosphere, Atmos. Chem. Phys., 11, 12813–12837, 2011.

Peischl, J, et al., Quantifying sources of methane using light alkanes in the Los Angeles basin, California, J. Geophys. Res., 118, 4974-4990. 2013.

Peischl, J., et al., Quantifying atmospheric methane emissions from the Haynesville, Fayetteville, and northeastern Marcellus shale gas production regions. J. Geophys. Res., 120, 2119-2139, 2015.

Peischl, J., A. Karion, C. Sweeney, E. A. Kort, M. L. Smith, A. R. Brandt, T. Yeskoo, K. C. Aikin, S. A. Conley, A. Gvakharia, M. Trainer, S. Wolter and T. B. Ryerson,Quantifying atmospheric methane emissions from oil and natural gas production in the Bakken shale region of North Dakota, J. Geophys. Res., DOI: 10.1002/2015JD024631, 2016.

Polonsky, L.N., et al., Performance of a geostationary mission, geoCARB, to measure CO2, CH4 and CO column-averaged concentrations, Atmos. Meas. Tech., 7, 959–981, 2014.

Prather, M.J., Timescales in atmospheric chemistry: Theory, GWPs for CH_4 and CO, and runaway growth, Geophys. Res. Lett., 23, 2597–2600 1996.

Prather, M. J., C. D. Holmes, and J. Hsu: Reactive greenhouse gas scenarios: Systematic exploration of uncertainties and the role of atmospheric chemistry, Geophys. Res. Lett., 39, L09803, doi:10.1029/2012GL051440, 2012.

President's Climate Action Plan: Strategy to Reduce Methane Emissions, http://www.whitehouse.gov/sites/default/files/strategy_to_reduce_methane_emissions_2014-03-28_final.pdf, 2014.

Rayner, P.J., S.R. Utembe, and S. Crowell, Constraining regional greenhouse gas emissions using geostationary concentration measurements: a theoretical study, Atmos. Meas. Tech., 7, 3285–3293, 2014.

Remer, L.A., S. Mattoo, R. C. Levy, A. Heidinger, R. B. Pierce, and M. Chin, Retrieving aerosol in a cloudy environment: aerosol product availability as a function of spatial resolution, Atmos. Meas. Tech., 5, 1823–1840, 2012

Roberts, D.A., Bradley, E.S., Cheung, R., Leifer, I., Dennison, P.E. and Margolis, J.S., Mapping methane emissions from a marine geological seep source using imaging spectrometry. Remote Sensing of Environment,114, 592-606, 2010.

Rodgers, C.D.: Inverse Methods for Atmospheric Sounding, World Scientific Publishing Co., Singapore, 2000.

Saad, K.M., Derivation of tropospheric methane from TCCON CH4 and HF total column observations, Atmos. Meas. Tech., 7, 2907–2918, 2014.

Schepers, D., Guerlet, S., Butz, A., Landgraf, J., Frankenberg, C., Hasekamp, O., Blavier, J.-F., Deutscher, N.M., Griffith, D.W.T., Hase, F., Kyro, E., Morino, I., Sherlock, V., Sussmann, R., and Aben, I., Methane retrievals from Greenhouse Gases Observing Satellite (GOSAT) shortwave infrared measurements: Performance comparison of proxy and physics retrieval algorithms, J. Geophys. Res., 117, D10307, doi:10.1029/2012JD017549, 2012.

Schneising, O., J. P. Burrows, R. R. Dickerson, M. Buchwitz, M. Reuter, and H. Bovensmann, Remote sensing of fugitive methane emissions from oil and gas production in North American tight geologic formations, Earth's Future, 2, 548–558, 2014.

Shephard. M.W., et al., TES ammonia retrieval strategy and global observations of the spatial and seasonal variability of ammonia, Atmos. Chem. Phys., 11, 10743–10763, 2011.

Shephard, M.W., and K.E. Cady-Pereira, Cross-track Infrared Sounder (CrIS) satellite observations of tropospheric ammonia, Atmos. Meas. Tech., 8, 1323–1336, 2015.

Spahni, R., et al., Constraining global methane emissions and uptake by ecosystems, Biogeosciences, 8, 1643–1665, 2011.

Streets, D., T. Canty, G. Carmichael, B. de Foy, R. Dickerson,, B. Duncan, D. Edwards, J. Haynes, D. Henze, M. Houyoux, D. Jacob, N. Krotkov, L. Lamsal, Y. Liu, Z. Lu, R. Martin, G. Pfister, R. Pinder, R. Salawitch, and K. Wecht, Emissions estimation from satellite retrievals: A review of current capability, Atmos. Environ., 77, 1011–1042, 2013.

Thompson, D.R., Leifer, I., Bovensmann, H., Eastwood, M., Fladeland, M., Frankenberg, C., Gerilowski, K., Green, R.O., Kratwurst, S., Krings, T. and Luna, B., Real-time remote detection and measurement for airborne imaging spectroscopy: a case study with methane. Atmospheric Measurement Techniques, 8, 4383-4397, 2015.

Thorpe, A.K., C. Frankenberg, A.D. Aubrey, D.A. Roberts, A.A. Nottrott, T.A. Rahn, J.A. Sauer, M.K. Dubey, K.R. Costigan, C. Arata, A.M. Steffke, S. Hills, C. Haselwimmer, D. Charlesworth, C.C. Funk, R.O. Green, S.R. Lundeen, J.W. Boardman, M.L. Eastwood, C.M. Sarture, S.H. Nolte, I.B. Mccubbin, D.R. Thompson, and J.P. McFadden, Mapping methane concentrations from a controlled release experiment using the next generation airborne visible/infrared imaging spectrometer (AVIRIS-NG), Remote Sensing of Environment, 179, 104-115, 2016.

Tratt, D.M., Buckland, K.N., Hall, J.L., Johnson, P.D., Keim, E.R., Leifer, I., Westberg, K. and Young, S.J., 2014. Airborne visualization and quantification of discrete methane sources in the environment, Remote Sensing of Environment, 154, 74-88, 2014.

Turner, A.J. and D.J. Jacob, Balancing aggregation and smoothing errors in inverse models, Atmos. Chem. Phys., 15, 7039-7048, 2015.

Turner, A.J., D.J. Jacob, K.J. Wecht, J.D. Maasakkers, E. Lundgren, A.E. Andrews, S.C. Biraud, H. Boesch, K.W. Bowman, N.M. Deutscher, M.K. Dubey, D.W.T. Griffith, F. Hase, A. Kuze, J. Notholt, H. Ohyama, R. Parker, V.H. Payne, R. Sussmann, C. Sweeney, V.A. Velazco, T. Warneke, P.O. Wennberg, and D. Wunch, Estimating global and North American methane emissions with high spatial resolution using GOSAT satellite data, Atmos. Chem. Phys., 15, 7049-7069, 2015.

Turner, A.J., D.J. Jacob, J. Benmergui, S.C. Wofsy, J.D. Maasakkers, A. Butz, O. Hasekamp, S.C. Biraud, and E. Duglokencky, A large increase in US methane emissions over the past decade inferred from satellite data, Geophys. Res. Lett., 43, doi:10.1029/2016GL067987, 2016.

US EPA, Inventory of U.S. greenhouse gas emissions and sinks: 1990-2012, https://www3.epa.gov/climatechange/ghgemissions/usinventoryreport.html, 2016.

Van Damme, M., R. J. Wichink Kruit, M. Schaap, L. Clarisse, C. Clerbaux, P.-F. Coheur, E. Dammers, A. J. Dolman, and J. W. Erisman, Evaluating 4 years of atmospheric ammonia (NH_3) over Europe using IASI satellite observations and LOTOS-EUROS model results, J. Geophys. Res., 119, 9549–9566, 2014.

Veefkind, J.P., Aben, I., McMullan, K., Forster, H., de Vries, J., Otter, G., Claas, J., Eskes, H.J., de Haan, J.F., Kleipool, Q., van Weele, M., Hasekamp, O., Hoogeveen, R., Landgraf, J., Snel, R., Tol, P., Ingmann, P., Voors, R., Kruizinga, B., Vink, R., Visser, H., and Levelt, P.F., TROPOMI on the ESA Sentinel-5 Precursor: A GMES mission for global observations of the atmospheric composition for climate, air quality and ozone layer applications, Remote Sensing of Environment 120, 70-83, 2012.

Von Clarmann, T., et al., Retrieval of temperature, H_2O, O_3, HNO_3, CH_4, N_2O, $ClONO_2$ and ClO from MIPAS reduced resolution nominal mode limb emission measurements, Atmos. Meas. Tech., 2, 159–175, 2009.

Voulgarakis, A., et al., Analysis of present day and future OH and methane lifetime in the ACCMIP simulations, Atmos. Chem. Phys., 13, 2563–2587, 2013.

Wang, H., D.J. Jacob, M. Kopacz, D.B.A. Jones, P. Suntharalingam, J.A. Fisher, R. Nassar, S. Pawson, and J.E. Nielsen, Error correlation between CO_2 and CO as constraint for CO_2 flux inversions using satellite data, Atmos. Chem. Phys., 9, 7,313-7,323, 2009.

Wang, Y.-P., and S.T. Bentley, Development of a spatially explicit inventory of methane emissions from Australia and its verification using atmospheric concentration data, Atmos. Environ., 36, 4,985-4,975, 2002.

Wecht, K. J., D. J. Jacob, S. C. Wofsy, E. A. Kort, J. R. Worden, S. S. Kulawik, D. K. Henze, M. Kopacz, and V. H. Payne, Validation of TES methane with HIPPO aircraft observations: implications for inverse modeling of methane sources, Atmos. Chem. Phys., 12, 1823–1832, 2012.

Wecht, K.J., D.J. Jacob, C. Frankenberg, Z. Jiang, and D.R. Blake, Mapping of North America methane emissions with high spatial resolution by inversion of SCIAMACHY satellite data, J. Geophys. Res., 119, DOI: 10.1002/2014JD021551, 2014a.

Wecht, K.J., D.J. Jacob, M.P. Sulprizio, G.W. Santoni, S.C. Wofsy, R. Parker, H. Bösch, and J.R. Worden, Spatially resolving methane emissions in California: constraints from the CalNex aircraft campaign and from present

(GOSAT, TES) and future (TROPOMI, geostationary) satellite observations, Atm. Chem. Phys., 14, 8175-8184, 2014b.
Wennberg, P.O., et al., On the sources of methane to the Los Angeles atmosphere, Environ. Sci. Technol., 46, 9282-9289, 2012.
Wofsy, S. C.: HIAPER Pole-to-Pole Observations (HIPPO): finegrained, global-scale measurements of climatically important atmospheric gases and aerosols, Philos. T. Roy. Soc. A, 369, 2073–2086, 2011.
Wood, J.D., R.J. Gordon, and C. Wagner-Riddle, Biases in discrete CH_4 and N_2O sampling protocols associated with temporal variation of gas fluxes from manure storage systems, Agricultural and Forest Meteorology, 171–172, 295– 305, 2013.
Worden, H.M., M.N. Deeter, D.P. Edwards, J.C. Gille, and J.R. Drummond, Observations of near-surface carbon monoxide from space using MOPITT multispectral retrievals, J. Geophys. Res., 115, D18314, 2010.
Worden, J., S. Kulawik, C. Frankenberg, V. Payne, K. Bowman, K. Cady-Peirara, K. Wecht, J.-E. Lee, and D. Noone, Profiles of CH_4, HDO, H_2O, and N_2O with improved lower tropospheric vertical resolution from Aura TES radiances, Atmos. Meas. Tech., 5, 397–411, 2012.
Worden, J., et al., CH_4 and CO distributions over tropical fires during October 2006 as observed by the Aura TES satellite instrument and modeled by GEOS-Chem, Atmos. Chem. Phys., 13, 3679–3692, 2013.
Worden, J.R., et al., Quantifying lower tropospheric methane concentrations using GOSAT near-IR and TES thermal IR measurements, Atmos. Meas. Tech., 8, 3433–3445, 2015
Wunch, D., G. C. Toon, J-F. L. Blavier, R. A. Waschenfelder, J. Notholt, B. J. Connor, D. W. T. Griffith, V. Sherlock and P. O. Wennberg, The Total Carbon Column Observing Network, Phil. Trans. R. Soc. A, 369, 2087-2112, 2011.
Xi, X., V. Natraj, R. L. Shia, M. Luo, Q. Zhang, S. Newman, S. P. Sander, and Y. L. Yung, Simulated retrievals for the remote sensing of CO_2, CH_4, CO, and H_2O from geostationary orbit, Atmos. Meas. Tech., 8, 4817–4830, 2015.
Xiao, Y, D.J. Jacob, J. Wang, J.A. Logan, P.I. Palmer, P. Suntharalingam, R.M. Yantosca, G.W. Sachse, D.R. Blake, D.G. Streets, Constraints on Asian and European sources of methane from CH_4-C_2H_6-CO correlations in Asian outflow, J. Geophys. Res., 109, D15S16, 2004.
Xiong, X., C. Barnet, E. Maddy, C. Sweeney, X. Liu, L. Zhou, and M. Goldberg, Characterization and validation of methane products from the Atmospheric Infrared Sounder (AIRS), J. Geophys. Res., 113, G00A01, doi:10.1029/2007JD000500, 2008.
Xiong, X., C. Barnet, E. S. Maddy, A. Gambacorta, T. S. King, and S. C. Wofsy, Mid-upper tropospheric methane retrieval from IASI and its validation, Atmos. Meas. Tech., 6, 2255-2265, doi:10.5194/amt-6-2255-2013, 2013.
Zavala-Araiza, D., et al., Toward a functional definition of methane super-emitters: application to natural gas production sites, Environ. Sci. Technol., 49, 8,167-8,174, 2015.
Zhang, L., D. J. Jacob, X. Liu, J. A. Logan, K. Chance , A. Eldering, and B. R. Bojkov, Intercomparison methods for satellite measurements of atmospheric composition: application to tropospheric ozone from TES and OMI, Atmos. Chem. Phys., 10, 4,725-4,739, 2010.
Zhao, C., A.E. Andrews, L. Bianco, J. Eluszkiewicz, A. Hirsch, C. MacDonald, T. Nehrkorn, and M.L. Fischer, Atmospheric inverse estimates of methane emissions from Central California, J. Geophys. Res., 114, D16302, 2009.
Zhu, L., D. K. Henze, K. E. Cady-Pereira, M. W. Shephard, M. Luo, R. W. Pinder, J. O. Bash, and G.-R. Jeong, Constraining U.S. ammonia emissions using TES remote sensing observations and the GEOS-Chem adjoint model, J. Geophys. Res., 118, 3355–3368, 2013.
Zoogman, P., D.J. Jacob, K. Chance, X. Liu, A. Fiore, M. Lin, K. Travis, Monitoring high-ozone events in the US Intermountain West using TEMPO geostationary satellite observations, Atmos. Chem. Phys., 14, 6261-6271, 2014.

Table 1. Satellite instruments for measuring tropospheric methane[a]

Instrument	Agency[b]	Data period	Overpass time [local]	Fitting window [nm] (spectral resolution)	Pixel size [km^2][c]	Coverage[d]	Precision[e]	Reference
Low Earth Orbit[f]								
Solar backscatter								
SCIAMACHY	ESA	2003-2012	10:00	1630-1670 (1.4)[g]	30×60	6 days	1.5 %[h]	Frankenberg et al. (2006)
GOSAT[i]	JAXA	2009-	13:00	1630-1700 (0.06)	10×10	3 days[j]	0.7 %	Kuze et al. (2016)
TROPOMI	ESA, NSO	2017-	13:30	2310-2390 (0.25)	7×7	1 day	0.6%	Butz et al. (2012)
GHGSat	GHGSat, Inc.	2016-	09:30	1600-1700 (0.1)	0.05x0.05[k]	12×12 km^2 grid[l]	1-5%	Footnote[m]
GOSAT-2	JAXA	2018-	13:00	1630-1700, 2330-2380 (0.06)	10x10	3 days[j]	0.4%	Glumb et al. (2014)
CarbonSat	ESA	proposed		1590-1680 (0.3)	2×2	5-10 days	0.4%	Buchwitz et al. (2013)
Thermal emission								
IMG	MITI	1996-1997	10:30/22:30	7100-8300 (0.7)	8×8	along track	4%	Clerbaux et al. (2003)
AIRS	NASA	2002-	13:30/01:30	6200-8200 (7)	45×45	0.5 days	1.5 %	Xiong et al. (2008)
TES	NASA	2004-2011	13:30/01:30	7580-8850 (0.8)	5×8	along track	1.0 %	Worden et al. (2012)
IASI	EUMETSAT	2007-	09:30/21:30	7100-8300 (1.5)	12×12	0.5 days	1.2 %	Xiong et al. (2013)
CrIS	NOAA	2011-	13:30/01:30	7300-8000 (1.6)	14×14	0.5 days	1.5%	Barnet et al. (2014)
Active (lidar)								
MERLIN	DLR/CNES	2020-	13:30/01:30	1645.552/1645.846[n]	pencil	along track	1-2%[o]	Kiemle et al. (, 2014)
Geostationary								
GEO-CAPE[p]	NASA	proposed	continuous	2300 nm band	4×4[q]	1 hour[r]	1.0%	Fishman et al. (2012)
GeoFTS	NASA	proposed	continuous	1650 and 2300 nm bands	3×3[q]	2 hours[r]	<0.2%	Xi et al. (2015)
geoCARB	NASA	proposed	continuous	2300 nm band	4×5[q]	2-8 hours[r]	1.0%	Polonsky et al. (2014)
G3E	ESA	proposed	continuous	1650 and 2300 nm bands	2×3[s]	2 hours[r]	0.5%	Butz et al. (2015)

[a] Solar occultation and limb instruments measuring methane in the stratosphere are referenced in Sect. 3.2.

[b] ESA = European Space Agency; JAXA = Japan Aerospace Exploration Agency; NSO = Netherlands Space Office; MITI = Japan Ministry of International Trade and Industry; NASA = US National Aeronautics and Space Administration; EUMETSAT = European Organization for the Exploitation of Meteorological Satellites; DLR = German Aerospace Center; CNES = French National Center for Space Studies. GHGSat, Inc. is a private Canadian company.

[c] At the subsatellite point.

[d] Time required for full global coverage (low Earth orbit) or continental coverage (geostationary orbit). Solar backscatter and lidar instruments observe the full methane column with near-uniform sensitivity, while thermal emission instruments are limited to the middle/upper troposphere (Fig. 3). Solar backscatter instruments observe only in the daytime and over land (except for sunglint observations). Some instruments have no cross-track viewing capability ("along track") and thus observe only a narrow subsatellite swath.

[e] 1-σ uncertainty for single observations.

[f] All in polar sun-synchronous orbit, observing at a fixed time of day (see "overpass time" column).

[g] SCIAMACHYalso had a 2.3 μm band intended for operational methane retrievals (Gloudemans et al., 2008) but this was abandoned due to poor detector performance.

[h] Precision for 2003-2005 observations, after which the instrument degraded (Frankenberg et al., 2011). The average single-observation precision for the 2003-2012 record is 3-5% (Buchwitz et al., 2015).

[i] TANSO-FTS instrument aboard the GOSAT satellite. We refer to the instrument in the text as "GOSAT" following common practice.

[j] Repeated observations at 3 cross-track pixels about 260 km apart and with 260 km along-track separation. GOSAT can also adjust its pointing to observe specific targets.

[k] GHGSat's ground sampling distance is 23 m (512 pixels span the 12 km field of view), but imaging resolution is anticipated to be about 50 m (limited by telescope focus).

[l] With revisit time of 2 weeks.

[m] Unpublished information from GHGSat, Inc. Description of the GHGSat instrument can be found in Brakeboer (2015).

[n] On-line/off-line.

[o] Monthly average over 50 ×50 km^2 areas.

[p] Specifications from the proposed CHRONOS implementation of GEO-CAPE (https://www2.acom.ucar.edu/chronos).

[q] At roughly 30° latitude to observe North America and/or East Asia.

[r] Over a continental-scale domain.

[s] At roughly 50° latitude to observe central Europe.

Table 2. Nominal capability for observing regional and point sources of methane from space

Instrument[a]	Regional source quantification (Q =72 tons h^{-1} over 300×300 km^2)[b]	Point source detection threshold[c] (Q_{min} , tons h^{-1})
SCIAMACHY	1 year averaging time	68
GOSAT	1 year averaging time	7.1
TROPOMI	single pass (1 day)	4.2
GHGSat	NA[d]	0.25[e]
GOSAT-2	4 months averaging time	4.0
MERLIN	7 months averaging time[f]	NA
CarbonSat	single pass (5-10 days)	0.80
GEO-CAPE,	single pass (1 hour)	4.0
GeoFTS	single pass (2 hours)	0.61[g]
geoCARB	single pass (2-8 hours)	4.0
G3E	single pass (2 hours)	1.3

[a] See Table 1 for instrument specifications.
[b] example of the Barnett Shale region in Northeast Texas (Lyon et al., 2015)
[c] Smallest point source detectable in a single observing pass. Detectability scales as Q/U and is given here for a wind speed U = 5 km h^{-1}.
[d] Not applicable. GHGSat has a 12×12 km^2 viewing domain, designed to observe point sources.
[e] Assuming 5% precision.
[f] Assuming 1.5% precision[g] Assuming 0.2% precision.

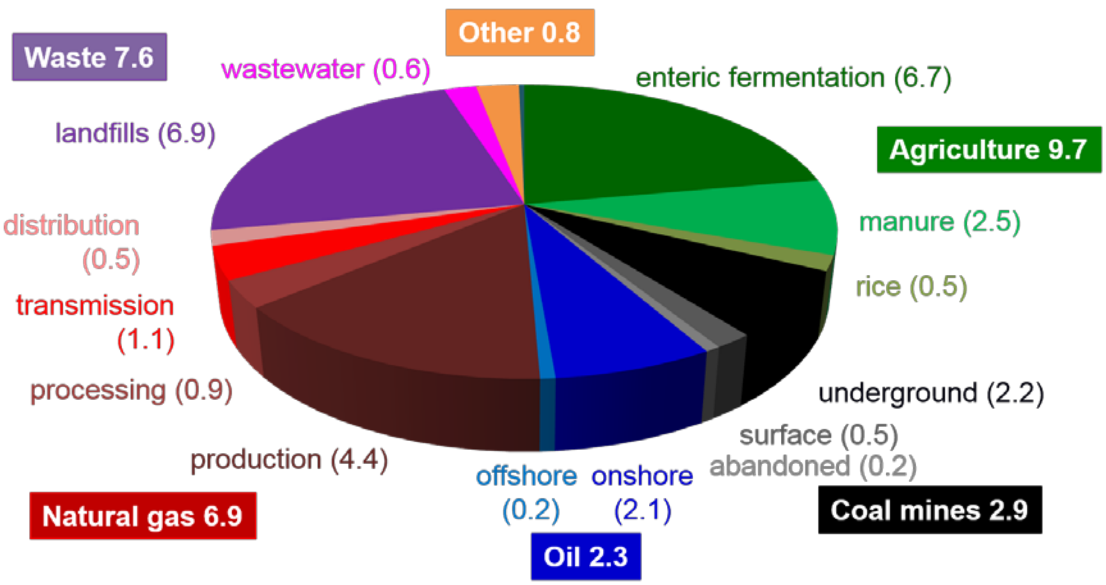

Figure 1. US national anthropogenic emission inventory for methane in 2012 compiled by the US EPA (2016). Units are Tg a^{-1}. "Other" sources include mainly fuel combustion (0.4 Tg a^{-1}) and open fires (0.4 Tg a^{-1}).

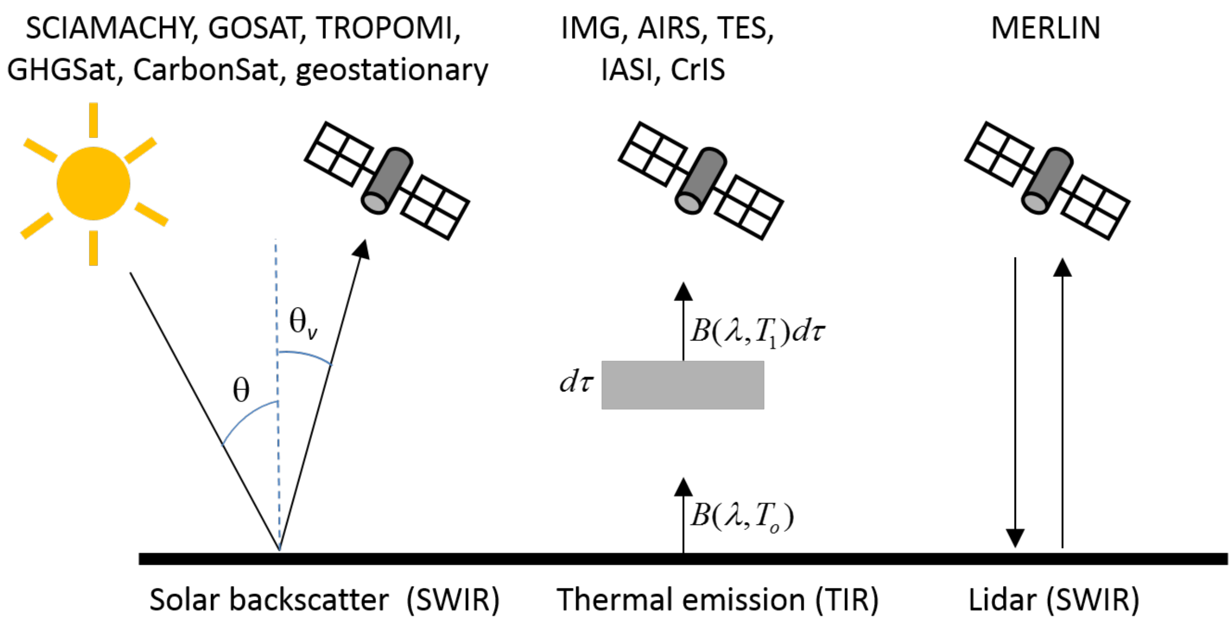

Figure 2. Configurations for observing methane from space in the shortwave infrared (SWIR) and in the thermal infrared (TIR). Here θ is the solar zenith angle, θ_v is the satellite viewing angle, $B(\lambda,T)$ is the blackbody function of wavelength λ and temperature T (T_o at the surface, T_1 at the altitude of the emitting methane), and $d\tau$ is an elemental methane optical depth. Satellite instruments operating in the different configurations are identified in the Figure and listed in Table 1.

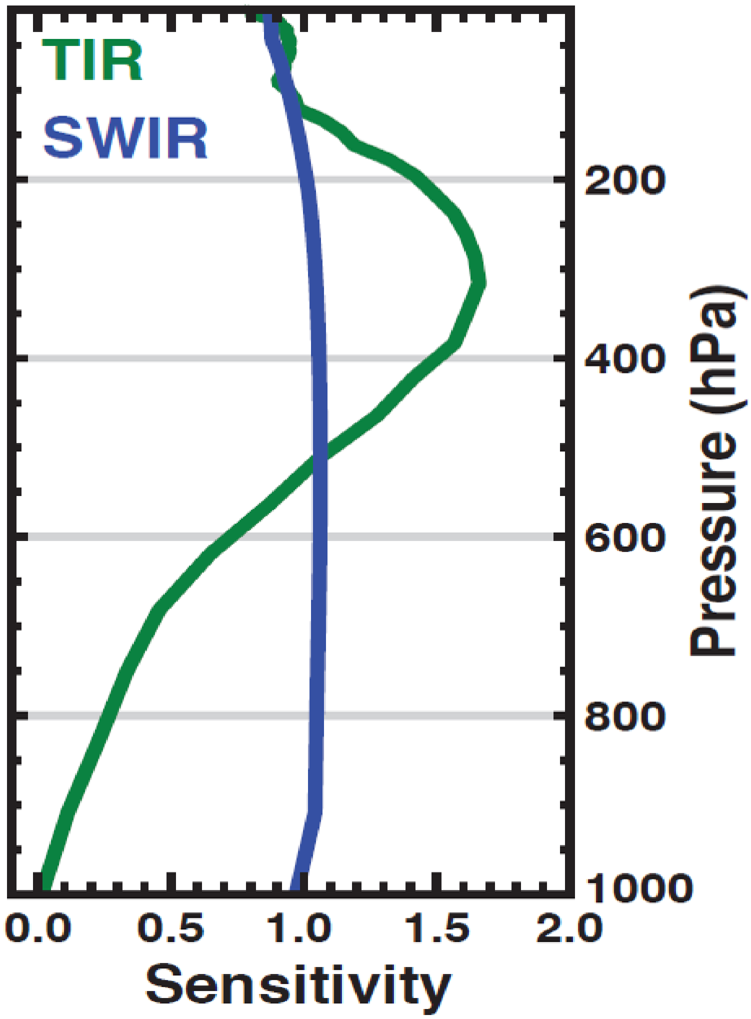

Figure 3. Typical sensitivities as a function of atmospheric pressure for satellite observation of atmospheric methane in the SWIR (solar back-scatter) and in the TIR. The sensitivities are the elements of the averaging kernel vector **a** at different pressure levels (Eq. (1)). Adapted from Worden et al. (2015).

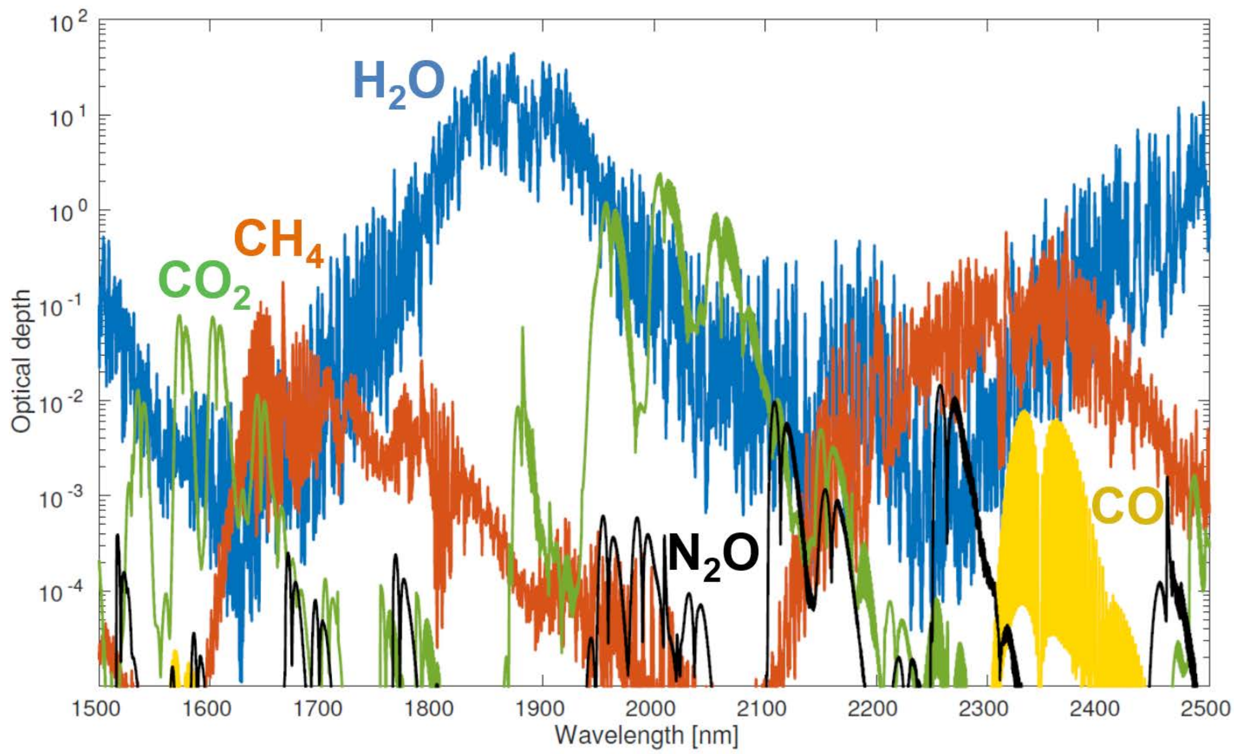

Figure 4. Atmospheric optical depths of major trace gases in the spectral region 1.5-2.5 μm. The calculation is for the US Standard Atmosphere (Anderson et al., 1986) with surface concentrations adjusted to 399 ppm CO_2, 1.9 ppm methane, 330 ppb N_2O, and 80 ppb CO. The line-by-line data have been smoothed with a spectral resolution of 0.1 nm (full width at half maximum).

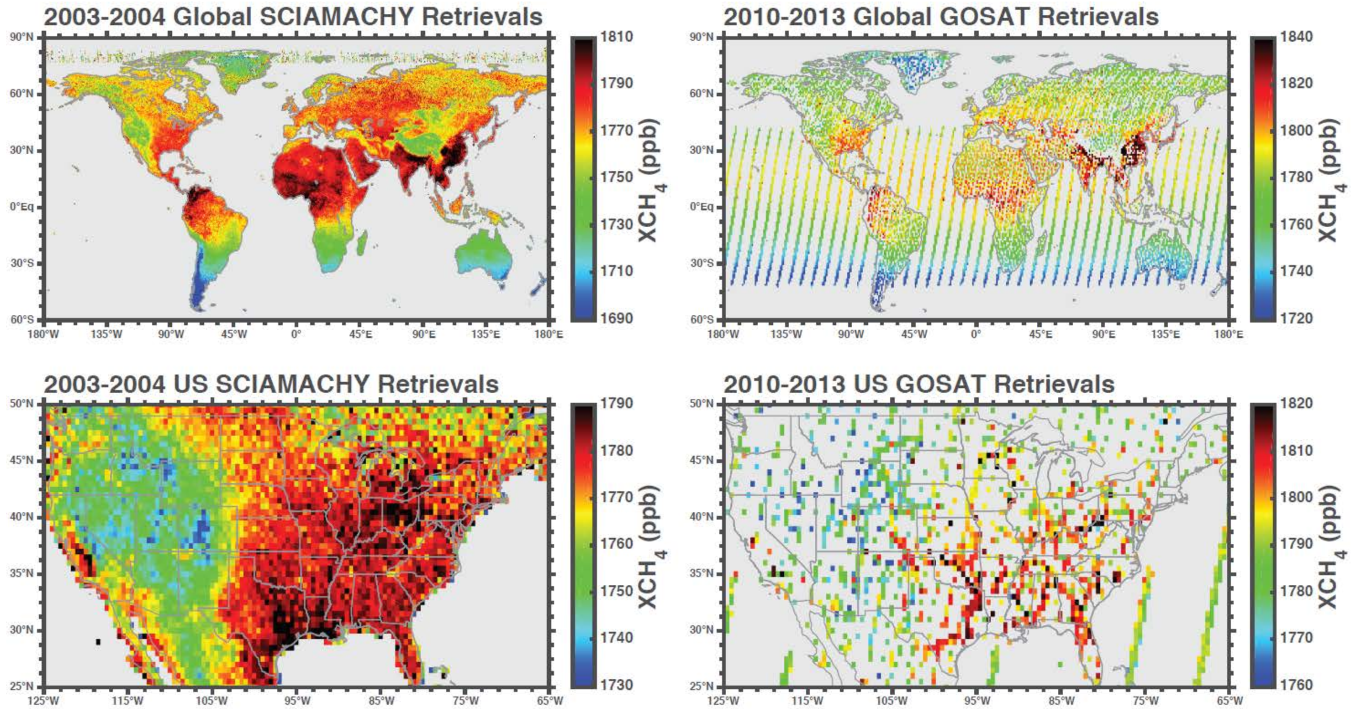

Figure 5. Global and US distributions of methane dry-air column mole fractions (X_{CH4}) observed by SCIAMACHY and GOSAT. Values are annual means for 2003-2004 (SCIAMACHY) and 2010-2013 (GOSAT), using the CO_2 proxy retrievals from Frankenberg et al. (2011) for SCIAMACHY and Parker et al. (2011) for GOSAT. GOSAT includes observations of sunglint over the oceans. The colorbar is shifted by 30 ppb between the SCIAMACHY and GOSAT panels to account for the global growth of methane from 2003-2004 to 2010-2013. All data are plotted on a 0.5°×0.5° grid except for the GOSAT global panel where a 1°×1° grid is used to improve visibility.

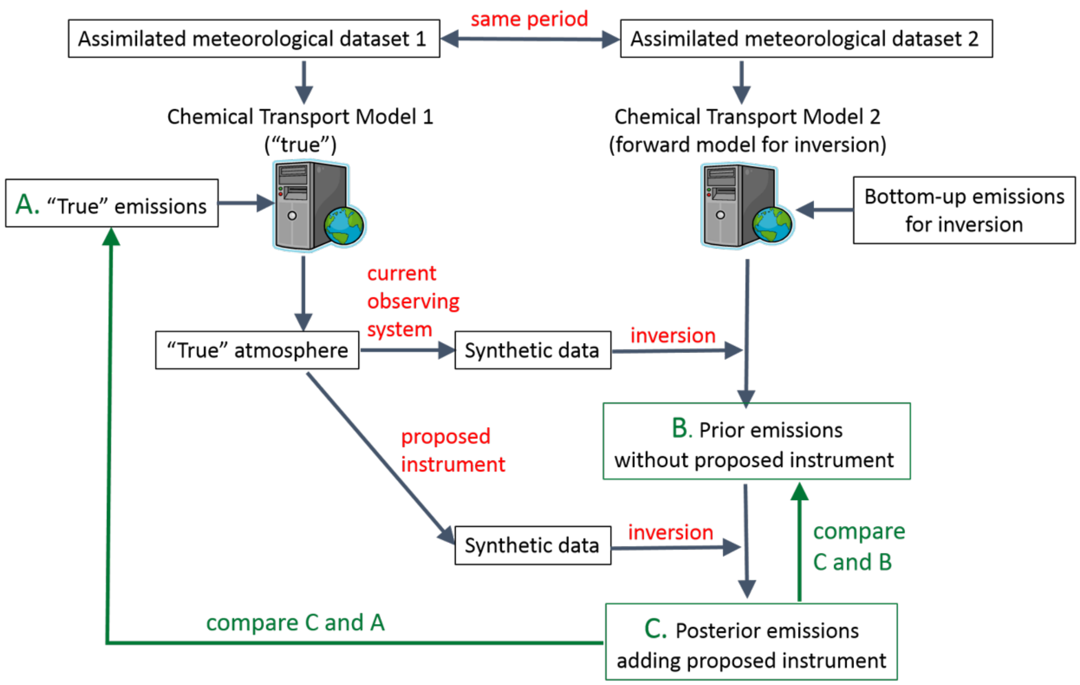

Figure 6. Generic design of an observing system simulation experiment (OSSE) to evaluate the potential of a proposed new atmospheric instrument to improve knowledge of emissions relative to the current observing system.

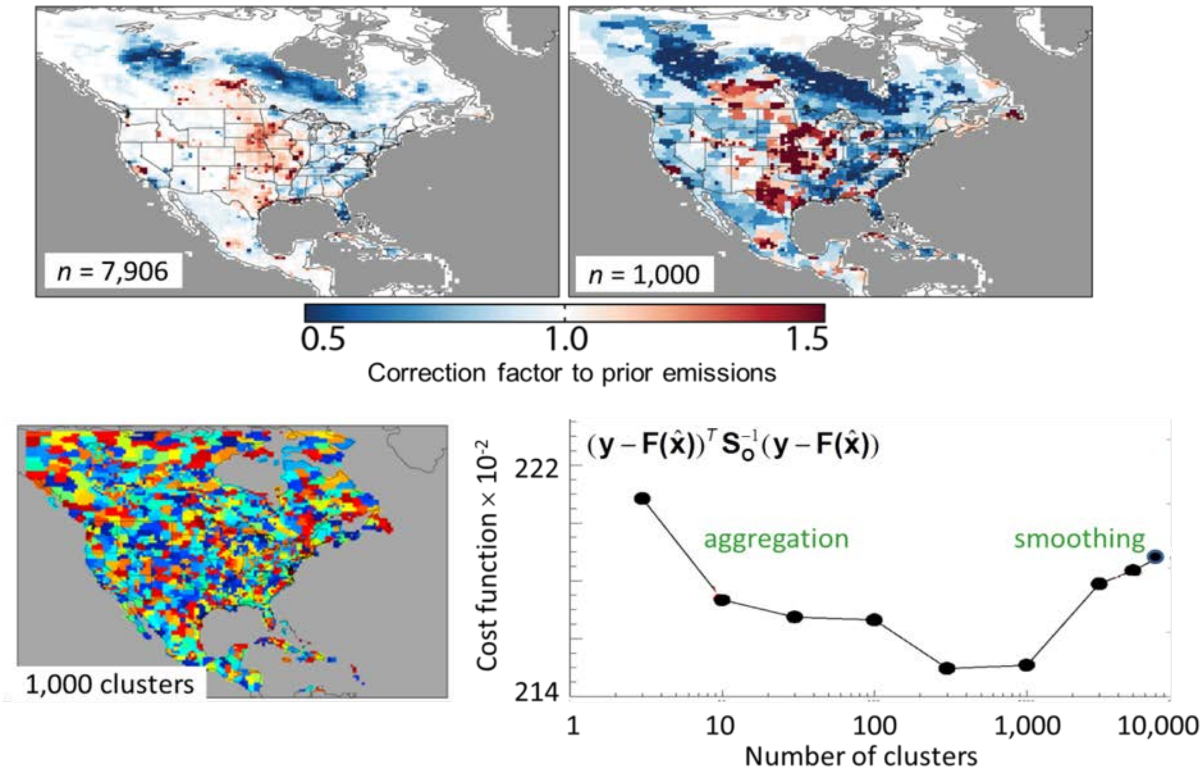

Figure 7. Effect of smoothing and aggregation errors in a high-resolution inversion of methane emissions using SCIAMACHY observations of methane columns for summer 2004. The top left panel shows the correction factors to prior emissions when attempting to optimize emissions at the native $1/2^{o}\times 2/3^{o}$ grid resolution of the chemical transport model (n = 7906). The top right panel shows the same inversion but with a reduced state vector (n = 1000) constructed by hierarchical clustering of the native-resolution grid cells (bottom left panel). The bottom right panel shows the ability of the inversion to fit the satellite observations as the state vector dimension is decreased from n = 7906 to n = 3 by hierarchical clustering. The quality of the fit is measured by the observational terms of the cost function for the inversion. Optimal results are achieved for n in the range 300-1,000. Finer resolution incurs large smoothing errors, while coarser resolution incurs large aggregation errors. Adapted from Wecht et al. (2014a).

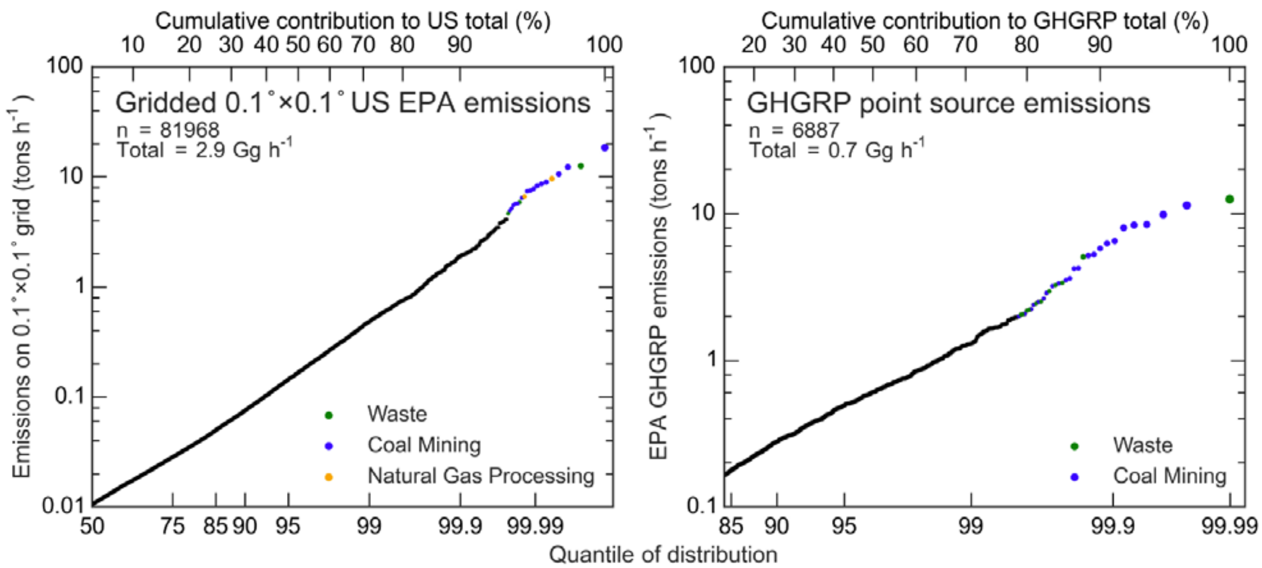

Figure 8. Cumulative frequency distribution of spatially resolved annual mean methane emissions in the contiguous US. The left panel shows the distribution of emissions at 0.1°×0.1° resolution in the gridded US EPA inventory for 2012 (Maasakkers et al., 2016). The right panel shows the distribution of point source emissions in the Greenhouse Gas Reporting Program (GHGRP) data for 2012. The highest sources are colored by sector. The x-axis is a normal cumulative probability scale such that a lognormal distribution would plot as a straight line. The cumulative relative contribution to the national total emissions is shown as the top axis. As an example of how to read these plots, the top 1% of GHGRP point source emissions (99th quantile in the right panel) includes n = 6887/99 = 69 point sources larger than 1.2 tons h^{-1} and contributes 29% of total US point source emissions in the GHGRP inventory.